The Anatomy of a Series of Cloud Bursts that Eclipsed the U.S. Rainfall Record

TERRENCE J. CORRIGAN JR.[a] AND STEVEN BUSINGER[a]

[a] *University of Hawai'i at Mānoa, Honolulu, Hawaii*

(Manuscript received 24 February 2021, in final form 5 December 2021)

ABSTRACT: A series of extreme cloudbursts occurred on 14 April 2018 over the northern slopes of the island of Kaua'i, Hawaii. The storm inundated some areas with 1262 mm (~50 in.) of rainfall in a 24-h period, eclipsing the previous 24-h U.S. rainfall record of 1100 mm (42 in.) set in Texas in 1979. Three periods of intense rainfall are diagnosed through detailed analysis of National Weather Service operational and special datasets. On the synoptic scale, a slowly southeastward propagating trough aloft over a deep layer of low-level moisture (>40 mm of total precipitable water) produced prolonged instability over Kaua'i. Enhanced northeast to east low-level flow impacted Kaua'i's complex terrain, which includes steep north- and eastward-facing slopes and cirques. The resulting orographic lift initiated deep convection. The wind profile exhibited significant shear in the troposphere and streamwise vorticity within the convective storm inflow. Evidence suggests that large directional shear in the boundary layer, paired with enhanced orographic vertical motion, produced rotating updrafts within the convective storms. Mesoscale rotation is manifest in the radar data during the latter two periods, and reflectivity cores are observed to propagate both to the left and to the right of the mean shear, which is characteristic of supercells. The observations suggest that the terrain configuration in combination with the wind shear separates the area of updrafts from the downdraft section of the storm, resulting in almost continuous heavy rainfall over Waipā Garden.

KEYWORDS: Flood events; Supercells; Orographic effects

1. Introduction

A series of intense thunderstorms, beginning around 0000 UTC 15 April 2018, impacted the north-central topography of Kaua'i, Hawaii, for over 24 h. The U.S. 24-h rainfall record was broken by this storm, with 1262 mm (~50 in.) measured at Waipā Garden (hereinafter referred to as Waipā) operated by the nonprofit Waipā Foundation, located within Hanalei Bay just north of Mount Wai'ale'ale (Figs. 1 and 2).

The unprecedented rainfall on the north slope of Kaua'i caused the Hanalei River to rise at least 2.4 m (8 ft) above the flood stage. The river jumped its banks and washed houses, cars, and bison into the ocean (Fig. 1a). Multiple landslides destroyed roads and bridges, isolating communities beyond Hanalei, with access limited to boat or helicopter. This storm cost the state over $54 million in damages, affecting over 500 residences, with over 150 homes destroyed, but fortunately it claimed no lives. As a result of the extensive damage and recovery operation, the popular tourist area was restricted to residents only for more than 8 months.

The Global Forecast System (GFS) and European Centre for Medium-Range Weather Forecasts (ECMWF) runs initialized 24 h prior to the event only forecast ~15.6 and 6.3 mm of rainfall, respectively, for northern portions of Kaua'i during the 24-h record period. The first flash flood warning for Kaua'i was issued at 0530 Hawaii standard time (HST) 14 April 2018. Operational model guidance was insufficient to allow for earlier warnings. The observed 24-h accumulation of 1262 mm (~50 in.) was a statistical anomaly with a recurrence interval >1000 years for northern Kaua'i (Perica et al. 2011). The previous U.S. 24-h rainfall record of 1100 mm (42 in.) occurred at Alvin, Texas, in 1979 as a result of a stalled tropical depression. The two prior rainfall records of 983 and 970 mm (38.7 and 38.2 in., respectively) were also associated with tropical moisture sources near the Gulf of Mexico. In comparing this rainfall event with record events globally, it is seen that the tropical deluge over Kaua'i lies near the global maximum 24-h rainfall given by a regression equation developed by Ramage (1995) (Fig. 3). All of the record events shown in Fig. 3 for storm totals >18 h were associated with tropical cyclones. The Kaua'i storm was unique in that it was a baroclinic system that produced multiple cases of terrain-anchored supercells. Significantly, this event was not associated with a tropical cyclone.

Kodama and Businger (1998) noted that the synoptic-scale disturbances that produce heavy rainfall in Hawaii can be classified into four synoptic systems: Kona lows; cold fronts; upper tropospheric troughs; and tropical cyclones. The Kaua'i rainfall event best fits the classification of an upper tropospheric trough. They also note that the Hawaiian Islands are prone to flash flooding as a result of small watersheds, shallow soils, and steep terrain. Hawaii's complex topography plays an integral role in instigating enhanced vertical motion, moisture-flux convergence, and terrain anchoring (Schroeder 1977; Murphy and Businger 2011; Robinson and Businger 2019).

Lin et al. (2001) noted that a significant amount of heavy orographic rainfall events occur over mesoscale mountain ranges. They separate the vertical motion in the moisture flux term into the environmental and orographic components. In their study, they note that that heavy orographic rainfall requires significant contributions from any combination of the following nine essential ingredients—L1: high precipitation efficiency, L2: presence of a moist low-level jet, L3: steep orography and L4: favorable mountain geometry, L5: abundant

Corresponding author: Steven Businger, businger@hawaii.edu

DOI: 10.1175/MWR-D-21-0028.1

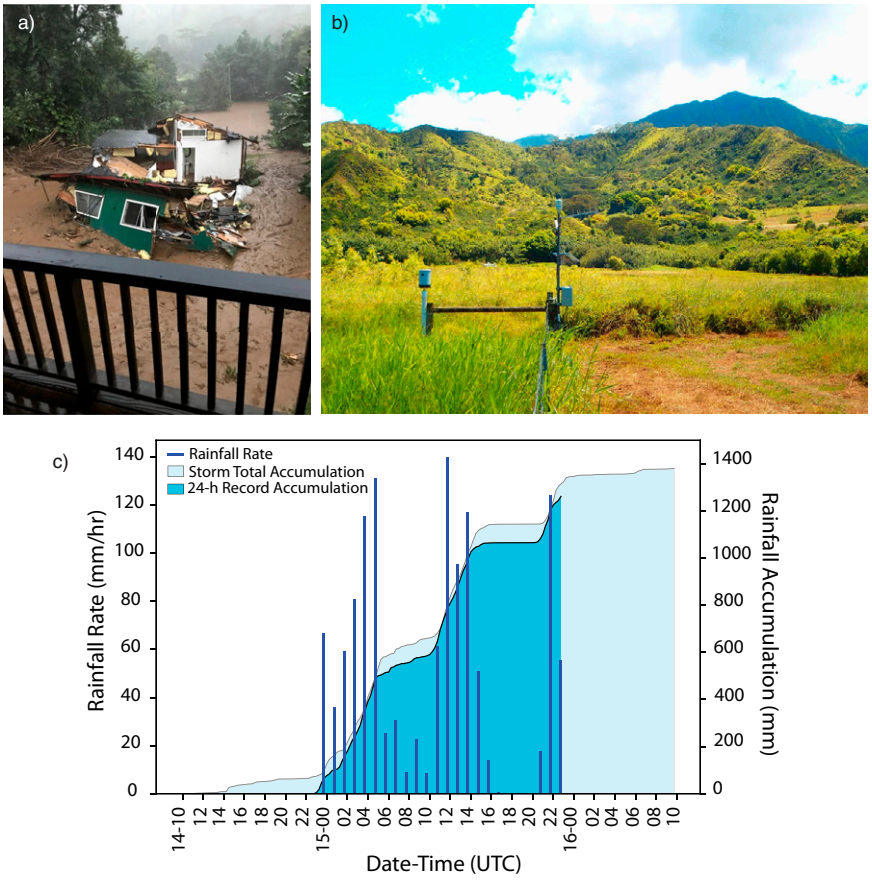

FIG. 1. (a) House destroyed by floodwaters near Waipā Garden. (b) Waipā Garden rain gauge with the northern slopes of Mount Wai'ale'ale in the background. (c) Time series of the Waipā Garden rain gauge showing hourly rainfall rate (histogram) and rainfall accumulation for the 24-h period beginning at 2245 UTC (1245 HST) 14 Apr 2018 (shaded blue) and the total storm (shaded light blue).

synoptic-scale moisture and L6: vertical motion upstream, L7: a slow-moving and L8: preexisting convective system, and L9: conditionally unstable airflow upstream. This study will show that the Kaua'i record storm included all nine of the essential ingredients in Lin et al. Labels L1–L9 are included in the text below to indicate when each of these ingredients is satisfied.

Kodama and Barnes (1997) studied 44 heavy rain events in Hawaii and noted a connection between the longevity and intensity of the rainfall to the magnitude of the vertical orographic motion, imparted from the grade of the terrain and magnitude of the moisture at midlevels in the troposphere. The moist midlevels are the result of horizontal moisture advection in the presence of large-scale rising motion associated with an approaching synoptic-scale disturbance, which acts to eliminate the trade wind inversion during the heavy rain events. Midlevel moisture reduces entrainment-driven dilution of cloud buoyancy and, therefore, allows for a deeper cloud with higher amounts of liquid water for precipitation processes (James and Markowski 2010; Morrison et al. 2020; Peters et al. 2020c). The enhancement of updrafts and suppression of downdrafts over terrain minimizes storm movement away from the terrain and favors terrain anchoring and subsequent high rainfall accumulations (Akaeda et al. 1995; Kodama and Barnes 1997).

Supercells are convective storms that are well known for their stable long-lived updrafts, persistent low-level mesocyclones, and exceptionally strong vertical velocities. Vertical pressure perturbations that arise as a result of the anomalous rotation in these systems can create comparable- or greater-magnitude vertical moisture fluxes into the storm than from buoyancy forces alone, increasing the rainwater mixing ratio, and energizing updrafts in these convective systems (Weisman and Klemp 1984; Weisman and Rotunno 2000). Further, Peters et al. (2019) showed that supercells also have larger buoyancy than non-supercells (all else being equal) because supercell updrafts are wider and experience less entrainment-driven dilution of buoyancy than non-supercells. Neilsen and Schumacher (2018) also showed that dynamic pressure perturbations associated with rotation in convection allow storms

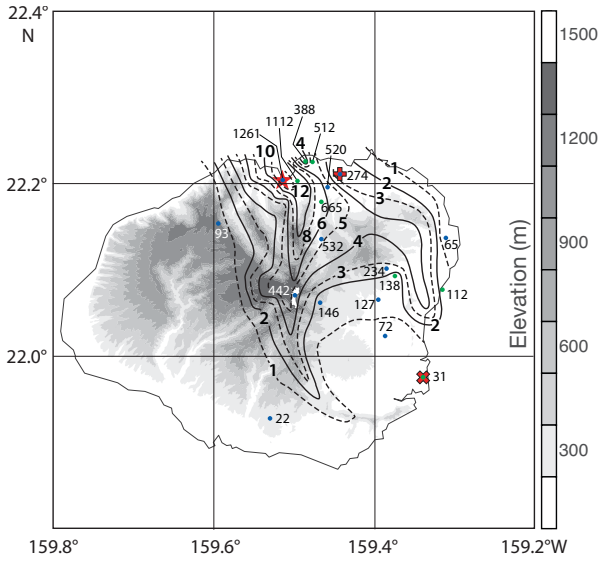

FIG. 2. Contour map of 24-h rainfall accumulation beginning at 2245 UTC 14 Apr 2018 (×100 mm). Waipā, Princeville Airport, and Lihue Airport are denoted by the red star, the red plus sign, and the red times sign, respectively. The blue-colored symbols indicate locations of METAR rain gauges, and the green symbols indicate locations of Weather Underground's "BestForecast" rain gauges, each with values in millimeters. USGS terrain elevation is shaded every 150 m.

to "access" a deeper inflow layer than would be available if rotation were absent, leading to greater precipitation production. As a result, case studies of supercell storms with strong low to midlevel rotation as well as tornadic storms have also been documented to produce record-breaking rainfall rates, especially within the warm sector of synoptic systems (Nielsen et al. 2015; Nielsen and Schumacher 2020a,b). Although rare for the Islands of Hawaii, supercell events do occur, bringing severe weather and torrential rains (Businger et al. 1998; Robinson and Businger 2019). An iconic case of a Hawaiian supercell occurred on the 9 March 2012 over the Ko'olau mountains of O'ahu and produced 108-mm hail and two tornadoes that impacted windward O'ahu (Robinson and Businger 2019).

This paper investigates the extreme rainfall event that occurred over the state of Kaua'i during the period 13–15 April 2018, which resulted in a record-setting ~1262 mm (~50″) rainfall over Waipā in 24 h. Section 2 presents data and methods. Section 3 documents the synoptic-scale context of this event. Section 4 documents the mesoscale components that contribute to the event's intensity and longevity. Conclusions and discussion are presented in section 5.

2. Data and methods

Analyses from the National Centers for Environmental Prediction (NCEP) GFS numerical model were utilized to provide an overview of the synoptic evolution of the rainfall event. The analysis dataset is available four times daily (1000, 1600, 2200, and 0400 HST) with horizontal resolution of 2.5°. Fine-resolution 10-m (0.0005°) terrain data from the U.S. Geological Survey (USGS) are implemented to investigate the complex role that terrain has on storm initiation, anchoring, and intensification.

Four dual-polarized WSR-88D instruments are administered by the Federal Aviation Administration and operated by the National Weather Service to cover the five international airports in Hawaii. The radar station used for this

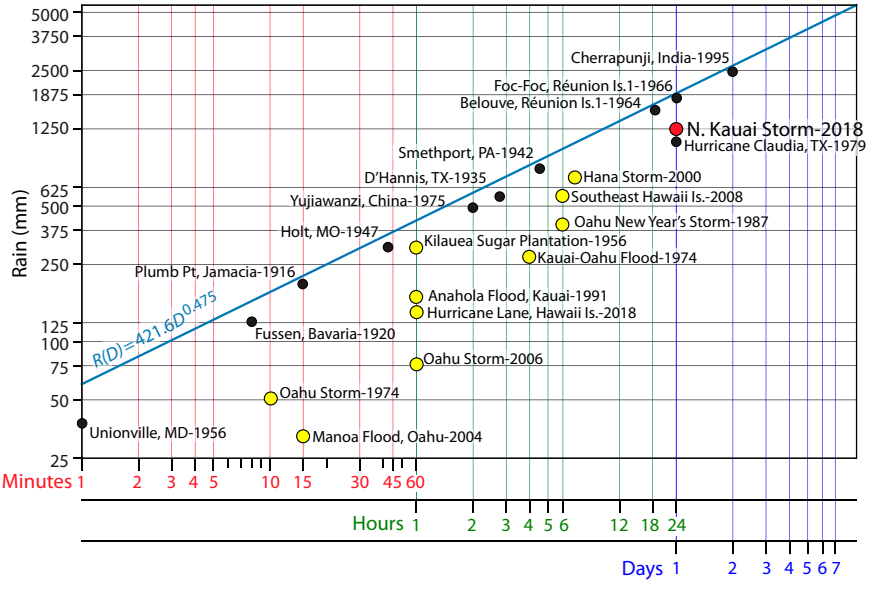

FIG. 3. World-record rainfall events (accumulations in millimeters) as a function of duration (after Ramage 1995). Notable Hawaiian rainfall records are in yellow, and the 24-h Kaua'i rainfall record event is in red.

analysis is the PHKI radar station located on the south shore of Kaua‘i at 21°53′39″N, 159°33′08″W. Products of reflectivity, radial velocity, and differential phase were analyzed with a pulse volume resolution of roughly 1 km in azimuth and 0.5 km in range over the Waipā area with a temporal resolution ranging from 4 to 5 min. For our study, only scan angles at and above 3.81° or ~2.5 km (800–750 hPa) above northern Kaua‘i are used in the rainfall analysis because of beam blocking by the central topography of Mount Wai‘ale‘ale. To estimate rainfall accumulation, the Rosenfeld reflectivity–rainfall (Z–R) relationship ($Z = 250R^{1.2}$) for deep tropical convection was applied to the lowest available radar scan level of reflectivity without beam attenuation (3.81°) (Rosenfeld et al. 1993). Because the freezing level was well above 3.5 km and, thus, above the scan 3.81° angle over Waipā, higher reflectivities known to be associated with frozen precipitation particles did not affect the radar analysis.

To construct vertical wind profiles during the storm period the velocity azimuthal display (VAD) technique is applied to Doppler radar data from station PHKI. Radar returns at a scan angle of 2.9° were analyzed below 1-km elevation for azimuthal angles ranging from 90° to 270°, corresponding to scans primarily over the water and thus away from terrain. This approach reduced the potential for errors in the horizontal wind estimates from stronger terrain induced updrafts.

The radar specific differential phase K_{DP} was also investigated; K_{DP} is directly proportional to liquid water content and has a linear relationship to rain rate (Kumjian and Ryzhkov 2009; Sachidananda and Zrnić 1987). The K_{DP} is negligible (~0) for spherical or tumbling particles, such as dry hail, and is a function of the drop size and concentration of the liquid water falling (Kumjian 2013); K_{DP} has been documented to produce more accurate rainfall accumulation in the presence of partial beam blockage as compared with reflectivity-derived rainfall accumulation (Brandes et al. 2001). The K_{DP} is also very effective at detecting regions of dense coalescence of water droplets and high liquid water content. This makes it an effective tool at estimating high rainfall accumulation observed in cloudbursts associated with large mesocyclones and high precipitation storms (Nielsen and Schumacher 2018). In addition, the highly sheared environment common to these storms can promote “size sorting” where larger diameter droplets fall faster and are thereby exposed to storm winds for a shorter period relative to smaller-sized droplets that are more susceptible to longer fall times and greater advection (Kumjian and Ryzhkov 2009). A greater spatial accuracy is therefore achieved in high-wind-shear environments with higher values of K_{DP} due to the reduction of drift observed in larger rain drops (>2 mm), which have a unique signature in K_{DP} (Loney et al. 2002). The K_{DP} is estimated from level-II radar data and converted using a subtropical K_{DP}-to-rain-rate relationship[1] ($R = 40.56K_{DP}^{0.866}$) (Sachidananda and Zrnić 1987).

Vaisala’s GLD360 lightning dataset was analyzed in this study (Said and Murphy 2016). The GLD360 lightning detectors measure cloud-to-ground (CG) and cloud-to-cloud (CC) lightning strokes, current, and polarity. The spatial accuracy of the GLD360 data is 300 ± 200 m, with a detection efficiency ranging from ~75% to 85%, depending on the time of day for the CG discharges, which are discerned within milliseconds (Said and Murphy 2016). Changes in the spatial distribution of lightning stroke density with time are a good proxy for radar reflectivity and rainfall rate, which has proven useful in areas where radar coverage is absent or limited (Pessi and Businger 2009; Stolz et al. 2014).

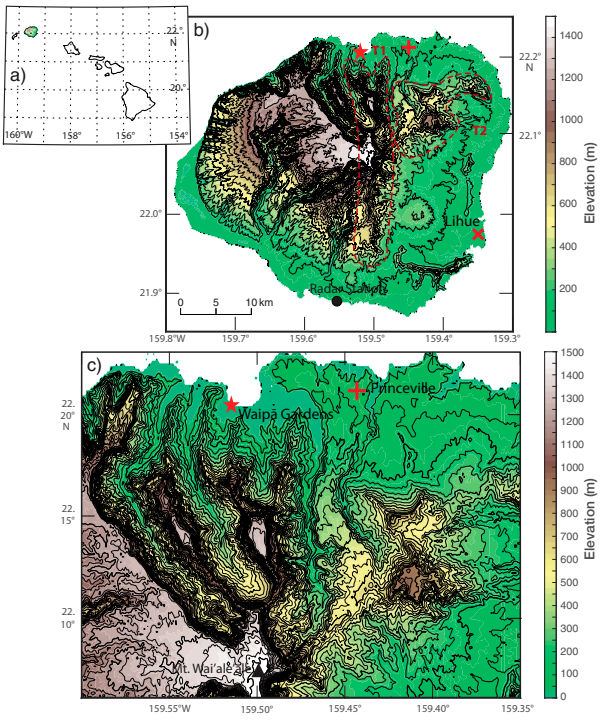

Fig. 4. (a) Map of the main Hawaiian Islands. (b) Topographic map of the island of Kaua‘i (contours every 100 m) showing the terrain features T1 and T2 referenced in the text. (c) Detail of Mount Wai‘ale‘ale and the northeast portion of Kaua‘i with height contours every 50 m. Station symbols are as in Fig. 2.

Radiosondes deployed twice daily at 0200 and 1400 HST from the Lihue Airport are used to document the wind and thermodynamic profiles of the atmosphere throughout this rainfall event. The proximity of Lihue to Waipā and its location on the east coast of Kaua‘i, make the profiles reasonably representative of synoptic conditions over Kaua‘i given the low-level easterly flow coming off of the ocean during the event (Fig. 4). Surface observations utilized in the rainfall analysis are shown in Fig. 2 and include two Automated Surface Observing System stations at Lihue and Princeville Airport.

Precipitation efficiency (PE) has been used in many past observational studies to characterize overall rain production; PE can be defined as the total rainfall measured at the ground divided by total water vapor flux into the storm. Through numerical simulation, patterns of high PE have been related

[1] K_{DP} was estimated using the Colorado State University CSU_Radartools code package.

to convective available potential energy (CAPE), boundary layer moisture, and magnitude of shear in storm environments (Weisman and Klemp 1982). To estimate the PE in the Kaua'i event, CAPE and magnitude of the cloud-layer shear from the Lihue sounding are utilized. The top of the storm layer is defined by the height of the >40-dBZ reflectivity in radar data during the event.

Storm-relative helicity (SRH) quantifies the degree of horizontal vorticity that exists within the storm-relative (SR) inflow. SRH is the vector product of the horizontal vorticity and the storm-relative winds or the scalar product of the magnitude of the SR inflow and the horizontal vorticity oriented along the SR inflow or streamwise vorticity ω_s. Enhanced values of streamwise vorticity occur when environmental winds strongly veer with height and often precede more organized and severe convection, such as mesocyclones and supercells, when the horizontal vorticity is tilted and stretched into the vertical by storm updrafts (Davies-Jones 1984). Environments with large low-level streamwise vorticity have been shown to contribute significantly to the vertical fluxes of boundary layer momentum, heat, and moisture, as well as to increase the low-level vertical motion and rotation of storm updrafts (Alpers and Brümmer 1994; Morrison et al. 2005; Peters et al. 2020a).

SR wind greater than 10 m s^{-1} is a threshold that is a necessary condition for supercells (Droegemeier et al. 1993). Enhanced SR inflow has been connected to maximum updraft velocity, increased vertical mass flux, and larger updraft width, making the updraft less susceptible to entrainment driven dilution of core buoyancy, and thus fostering longer-lived convection (Peters et al. 2019, 2020a,b). Significantly, it has been demonstrated that the magnitude of SR inflow is more important than the magnitude of storm-relative helicity in determining whether supercellular storm mode manifests (Peters et al. 2020a,b).

Combining the magnitude of SR inflow and the streamwise vorticity into SRH is an attractive method for capturing both the effects of supercell evolution and its interaction with the planetary boundary layer. Applying SRH to the lowest 500 m of the storm inflow has been shown to be strong predictor for differentiating tornadic from non-tornadic thunderstorms (Thompson et al. 2007; Coffer et al. 2019). Tornadic thunderstorms that exhibit large SRH are also commonly associated with heavy rainfall and flashflood events (Nielsen et al. 2015). Dynamic pressure perturbations linked to large SRH act to lower the level of free convection (LFC), which leads to greater precipitation production (Nielsen and Schumacher 2018).

SRH can be expressed as follows:

$$\mathrm{SRH} = \int_{z=z_1}^{z=z_2} \mathbf{V}_{\mathrm{SR}} \cdot \nabla \times \mathbf{V}\, dz = \int_{z=z_1}^{z=z_2} \omega_s |\mathbf{V}_{\mathrm{SR}}|\, dz$$

$$= \int_{z=z_1}^{z=z_2} \mathbf{k} \cdot \mathbf{V}_{\mathrm{SR}} \times \mathbf{S}\, dz, \qquad (1)$$

where $\mathbf{V}_{\mathrm{SR}}$ are the storm-relative winds composed as the difference between environmental winds $\mathbf{V}$ and the storm motion vector $\mathbf{c}$. The environmental horizontal vorticity component along the storm-relative velocity direction or streamwise direction is ω_s, and the mean environmental bulk wind shear is as follows: $\mathbf{S} = (\partial\overline{u}/\partial z)\mathbf{i}$, $(\partial\overline{v}/\partial z)\mathbf{j}$. This equation is integrated over the depth of the storm inflow (z_1, z_2) often taken between 0 and 1 km or between 0 and 3 km, respectively.

3. Synoptic-scale overview

The synoptic-scale conditions associated with this rainfall event are outlined in this section, noting that the primary focus of this paper is on the mesoscale. Two periods were selected to give an overview of the synoptic conditions. The first period is 1500 UTC 14 April, 12 h prior to convective initiation over Kaua'i and the second period is at 0900 UTC 15 April, during the peak convective activity of this storm (Figs. 5 and 6). The synoptic environment includes an upper-level low approaching Kaua'i (L8) from the northwest (Fig. 5). Upper-level lows are one of the four synoptic conditions conducive for enhanced rainfall and flooding for the Hawaiian Islands (Kodama and Businger 1998). Upper-level lows, which trace their origin in the polar jet stream farther north, often occur during the cool season (October–March) (Caruso and Businger 2006).

The approach of the upper-level low places the Hawaiian Islands under the right entrance of a jet streak aloft (Figs. 5a,b) (Uccellini and Kocin 1987). This region experienced positive vertical vorticity advection by the thermal wind, which is conducive to synoptic-scale ascent (L5) in the lower-to-middle troposphere (Figs. 6a,b) (Trenberth 1978). The synoptic-scale rising motion and cold-air advection associated with the upper-level trough act to erode the trade wind inversion (Figs. 5c,d). Climatologically, the tradewind inversion caps moist convection and mixing below an average height of ~2000 m over Kauai (Fig. 7) (Cao et al. 2007).

A weak inverted trough forms at the surface, consistent with ageostrophic forcing associated with the approaching upper-level low (Figs. 6c,d). The inverted trough causes the low-level (0–1 km) winds to shift direction from northeasterly to easterly in time while maintaining trade-wind strength (>10 m s^{-1}) (Fig. 7). The resulting back trajectory takes the surface air over warmer ocean water, since ocean temperatures in the central North Pacific Ocean decrease northward, thus moistening the boundary layer. The inverted trough also promotes surface convergence and lifting through Ekman pumping, which helps to saturate the boundary layer (L6) and fuel deepening convection (Figs. 6c,d).

4. Mesoscale analysis

In this section a mesoscale analysis of the 24-h period of heaviest rainfall over Waipā is presented. This analysis is separated into three distinct periods of extreme rainfall (see histogram in Fig. 1c)—P1: 1900 UTC 14 April–0800 UTC 15 April, P2: 0800–1900 UTC 15 April, and P3: 1900 UTC 15 April–0400 UTC 16 April. Unique thermodynamic and dynamic conditions, and orographic forcing characterize

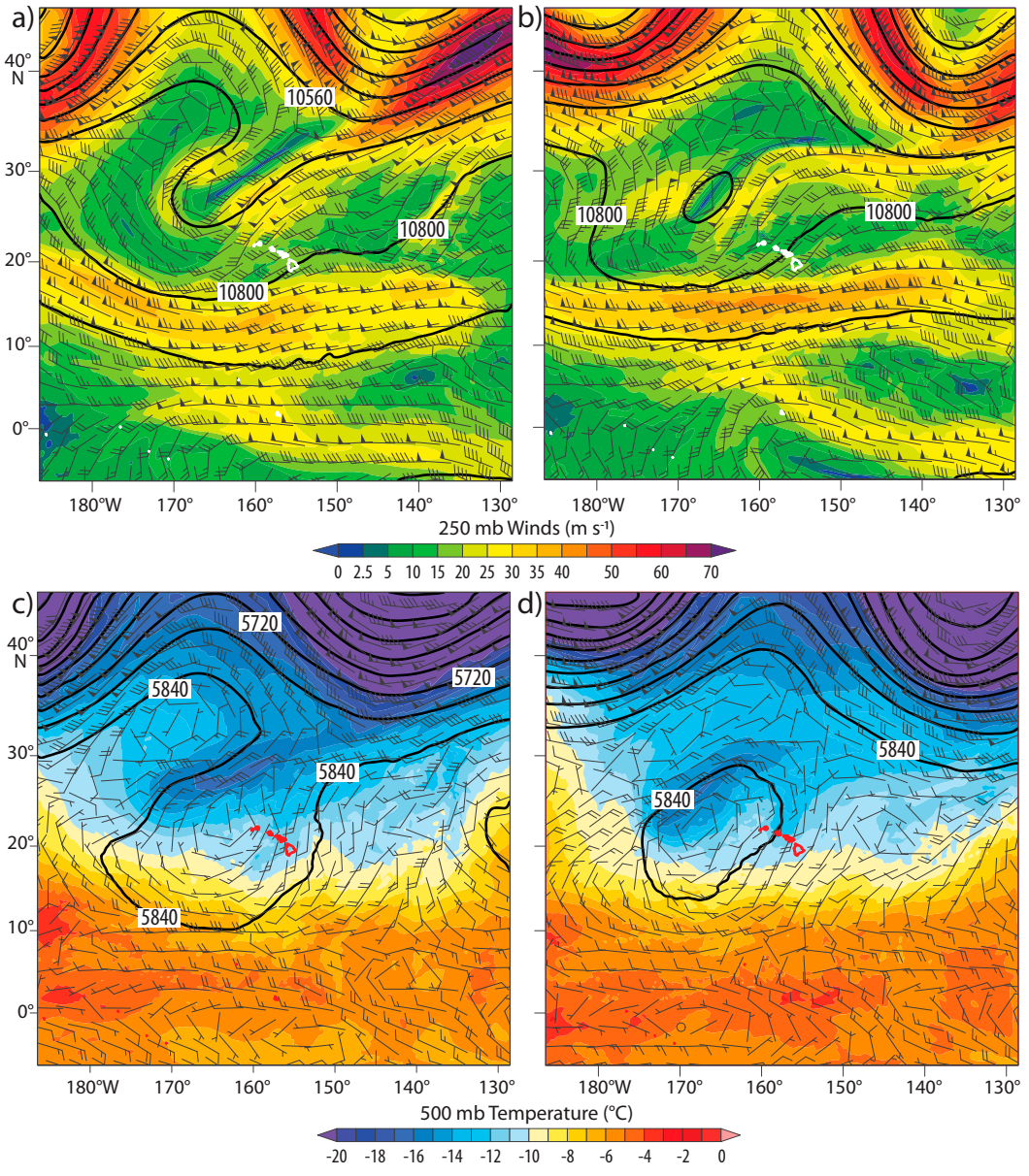

FIG. 5. NCEP–NCAR reanalysis dataset charts valid for (left) 1500 UTC 14 Apr and (right) 0900 UTC 15 Apr, showing (a),(b) the 250-hPa height contours (every 120 m), wind speed magnitude (shaded; m s^{-1}), and wind barbs plotted with the standard convention and (c),(d) the 500-hPa height contours (every 60 m), temperature (shaded; °C), and wind barbs plotted with the standard convention. The Hawaiian Islands are outlined in white in (a) and (b) and in red in (c) and (d).

each period. These elements combine to support the convective downbursts that broke the 24-h rainfall record at Waipā.

a. Period 1: 1900 UTC 14 April–0800 UTC 15 April

Prior to the onset of heavy rainfall during P1, the skew *T*–log*p* diagram at 1200 UTC 14 April already showed a conditionally unstable environment (L9) with a slight trade wind inversion near 2 km (Fig. 7a). At this time CAPE = 1642 J kg^{-1} and the LFC is located at ~962 hPa, just under 500 m, well below the summit of the local terrain (Fig. 4). The integrated water vapor value of 40 mm is 12 mm above the 28-mm average for Lihue (Foster and Bevis 2003). The maximum value observed during this storm (~42 mm) is much less than the maximum of ~70 mm observed during the Kaʻu storm, which produced a 24-h rainfall maximum of 940 mm (Foster et al. 2003).

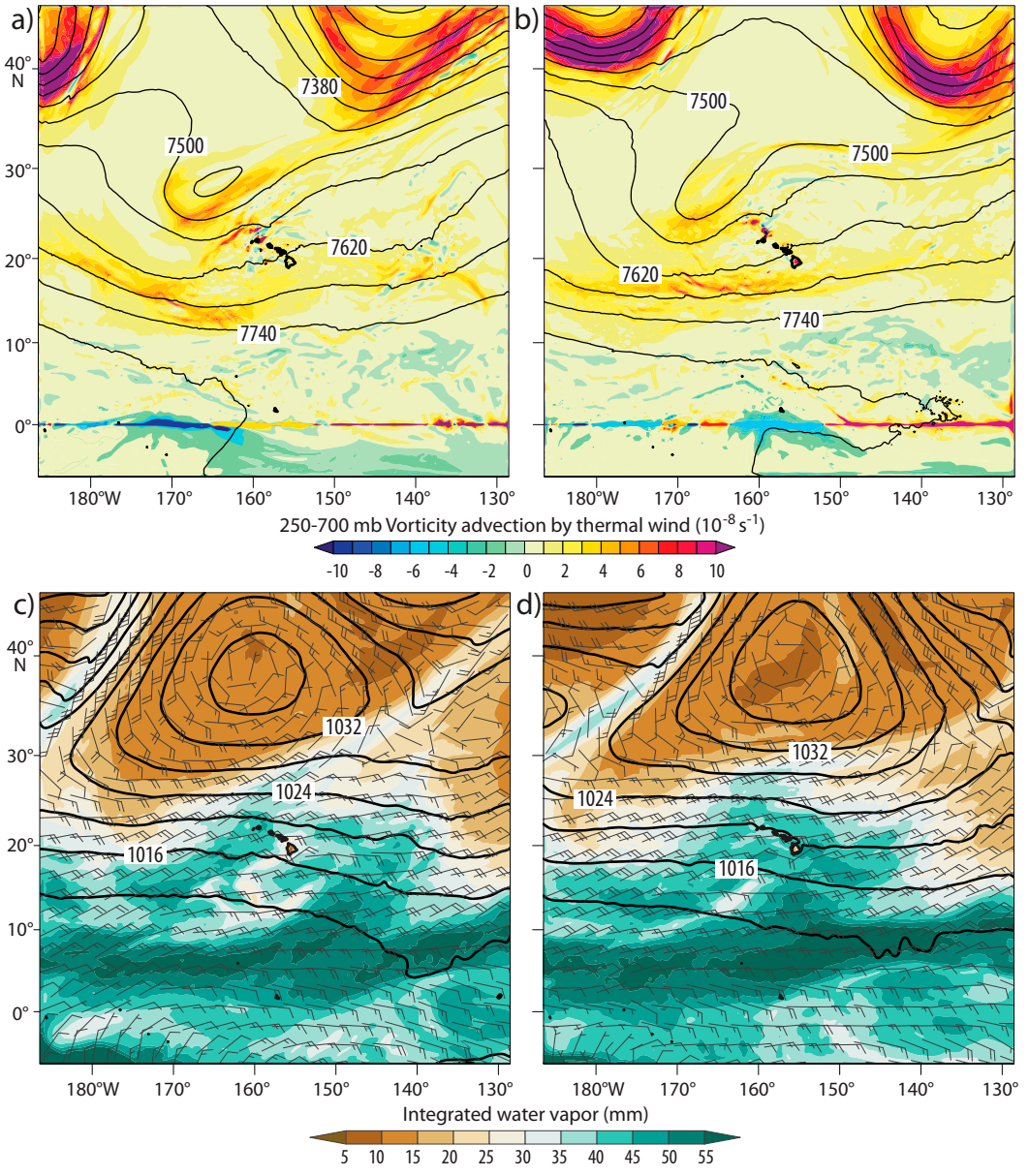

FIG. 6. NCEP–NCAR reanalysis charts for (left) 1500 UTC 14 Apr 2018 and (right) 0900 UTC 15 Apr 2018 for (a),(b) the 250–700-hPa geopotential thickness contours (every 60 m) and the vorticity advection by the thermal wind (shaded) and (c),(d) the 1000-hPa height contours (every 4 hPa), integrated water vapor (shaded; mm), and sea level wind barbs. The Hawaiian Islands are outlined in black.

At 0000 UTC 15 April, the midlevel (2–5 km) wind speeds increased, magnitude of trade wind inversion was reduced, and LFC lowered ~266 m to 981 hPa (Figs. 7b and 8b). The 0–3-km wind shear increased from ~5 to 15 m s^{-1} while the 0–6-km wind shear is observed to remain the same near 10 m s^{-1} (cf. Figs. 8a,b). Strong veering (clockwise turning) of the winds below 5 km indicates warm-air advection and is surmounted by a general backing of the winds with height from 5 to 9 km, suggesting cold-air advection. In sum, the differential advection contributes to conditional instability over the island of Kaua‘i (Fig. 8b).

During P1, the low-level horizontal inflow into terrain contains moderate values of storm-relative winds and helicity. Radar analysis, presented below, shows that the greatest reflectivity cores are largely terrain anchored. Therefore, SRH is derived by assuming the storm motion is set to zero [$\mathbf{c} = 0$ in Eq. (1)] and the storm-relative winds are just the environmental winds relative to the orographic updrafts from island terrain. A Froude number of 1.18 is calculated using the mean terrain height of ~1 km (T1 and T2), with the average stability and winds beneath this mean height sourced from sounding data at Lihue. This value is near the critical

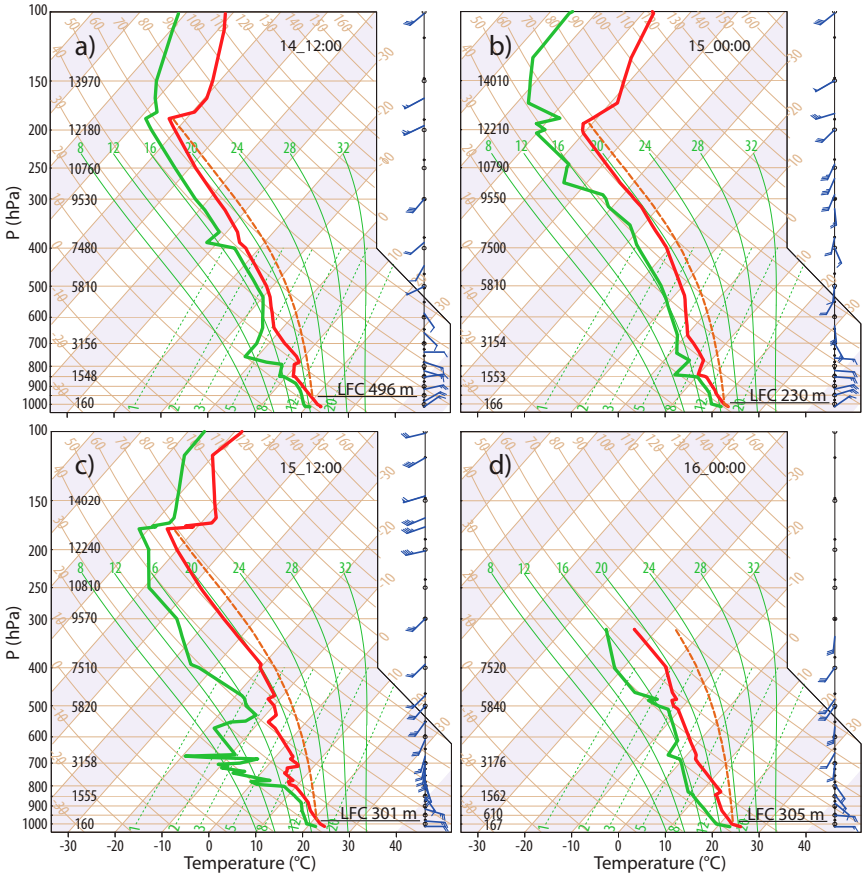

FIG. 7. Skew *T*–log*p* diagrams from Lihue Airport at (a) 1200 UTC 14 Apr, (b) 0000 UTC 15 Apr, (c) 1200 UTC 15 Apr, and (d) 0000 UTC 16 Apr, showing the environmental temperature profile (red) and dewpoint profile (green) and the parcel lapse rate (dashed orange). Wind barbs are plotted with the standard convention.

Froude number (1.0) that is conducive for terrain-anchored storms, which were observed during this period.

The average storm-relative wind within the 0–1-km layer, estimated using the VAD technique, is ~11 m s^{-1} for the duration of P1 and is greater than the threshold of storm-relative winds for supercell storms (Droegemeier et al. 1993; Peters et al. 2020a) (Fig. 9a). The majority of the 0–1-km winds are from the east-northeast (~65°) (Fig. 9b), which favors initiation of terrain-anchored storms along east-northeast-facing slopes of T2 and T1 as shown in the radar analysis discussed below. Both the 0–1-km wind direction and magnitude are in agreement with vertical wind profiles from Lihue sounding data. Moreover, the data show that a local low-level wind maximum, which satisfies the historical definition of a low-level jet (L2), is oriented normal to the terrain (Bonner 1968) (Figs. 8b and 9a,b).

The terrain-anchored SRH within the storm inflow layer from 0 to 1 km and from 0 to 3 km nearly doubles to 114 m^2 s^{-2} and to 194 m^2 s^{-2}, respectively, relative to the previous 12 h. Both values exceed the thresholds of SRH observed in mesocyclone and supercell environments (Thompson et al. 2007) (Fig. 9c).

Convective cells with reflectivity of at least 55 dB*Z* consistently originate from T2 and T1 throughout P1.[2] Radar reflectivity loops show precipitation advection toward the northwest, consistent with the mean wind in the 0–6-km layer, extending heavy rainfall over Waipā (Figs. 8b and 10a). The consistency of these convective cells in proximity of terrain suggests that terrain anchoring was an important mechanism in rainfall production at Waipā during P1.

During P1, a PE of ~40% (L1) is estimated from a CAPE of 1600 J kg^{-1} and an average convective cloud-layer (0–8 km) shear of 15 m s^{-1} (Weisman and Klemp 1982). Reflectivity data and radial velocity data both show evidence of weak circulation within convective cores via small and sporadic velocity couplets in areas of greater reflectivity just to the North of Waipā (latitude 22.3°, longitude −159.5°) (Figs. 10a,b). These rotating features seem to spin up downshear of T2 in the direction of the

[2] A radar loop is available at the following link to help readers visualize the reflectivity, circulations, and lightning discussed in the text (https://drive.google.com/drive/folders/1tSkhecCMPoHY198nIrt97Zc-t8WxBRlY?usp=sharing).

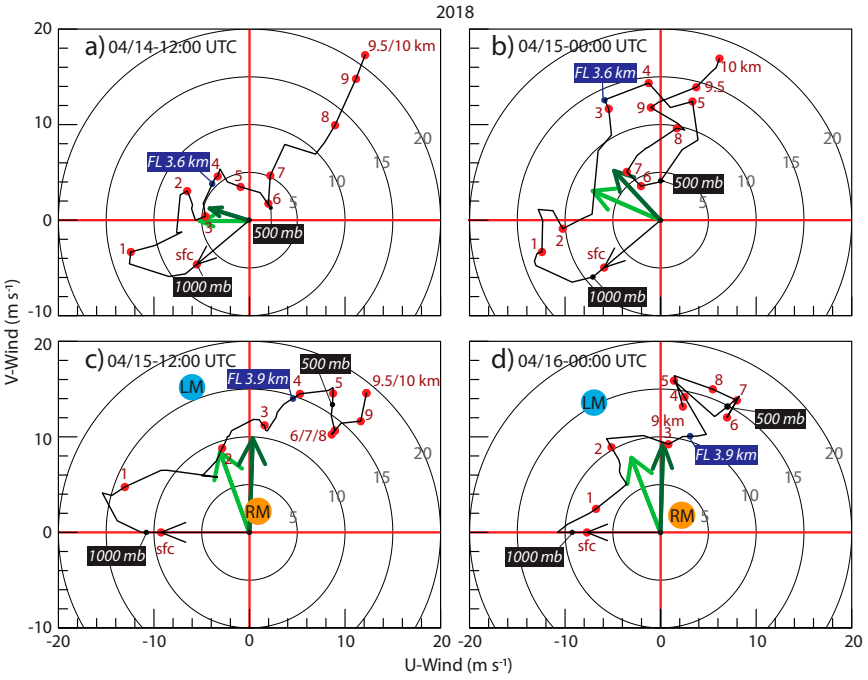

FIG. 8. Hodograph from Lihue Airport at (a) 1200 UTC 14 Apr, (b) 0000 UTC 15 Apr, (c) 1200 UTC 15 Apr, and (d) 0000 UTC 16 Apr. Light- and dark-green arrows correspond to the 0–6- and 0–10-km mean wind vectors, respectively; right and left storm motion are represented by the orange and blue circles, respectively; and the wind at the freezing level (FL) is indicated by the dark-blue labels.

mean wind in the 0–6-km layer from the southeast (Figs. 8b and 10b; see footnote 2).

During P1, a total of 2075 lightning strikes were observed, which represents 13% of the total lighting for the 24-h period of the rainfall record (Fig. 11a). The majority of the lightning strikes occur during the latter half of P1 (see footnote 2). Lightning strike density is well correlated with areas of enhanced circulation as well as with the rainfall accumulation for this period (Figs. 10b and 11a,b). The rainfall accumulation maximum for P2 of just over 700 mm consists of a very small and isolated area extending due north from Waipā (Fig. 11b).

The envelope of the coldest cloud tops at the end of P1 are oriented east-northeast following the winds above 13 km (Fig. 11a). Radar reflectivity data show that developing updrafts cores have yet to reach the equilibrium level (EL) (Figs. 7b and 10c) during P1. The envelope of the lightning strikes to the north of Waipā is consistent with southerly winds in the mixed phase region (Figs. 7b and 11a). The directional discrepancy between the envelope of the lightning strikes to the north and the envelope of cold cloud-top temperatures ($<-60°C$) oriented to the east-northeast (Fig. 11a) is consistent with the veering of the winds with height aloft during this period (Figs. 8b).

b. Period 2: 0800–1900 UTC 15 April

During P2, temperature and dewpoint profiles show significant moisture throughout the troposphere, an LFC at 980 hPa (300 m), the highest EL for all three periods (13 km), and CAPE = 1886 J kg^{-1} (Fig. 7c). The Lihue sounding shows an inflection point in the low-level (0–1 km) wind profile, which favors the presence of helical rolls in the boundary layer (Brown 1980; Bryan et al. 2007) (Fig. 8c). The maximum velocity of just over 15 m s^{-1} in the profile satisfies the criteria for supercell development (Raymond 1978). The hodograph shows veering of the winds with height and large directional wind shear from 1 to 10 km (Fig. 8c). The 0–3- and 0–10-km wind shears remain relatively unchanged from P1 with values of 15 and 30 m s^{-1}, respectively. However, the 0–6-km wind shear more than doubles from 9 to 21 m s^{-1}, exceeding the threshold of 20 m s^{-1} for supercell environments (Thompson et al. 2007) (Figs. 8b,c).

The 0–1-km distribution of storm-relative winds shows a narrower distribution in velocity in comparison with P1 (Fig. 9a), with a shift to a more easterly direction (Fig. 9b), which in turn shifts the orographic forcing to east-facing slopes, especially favoring T1 (L3 and L4) (Fig. 4). A Froude number of ~1 is found using the mean terrain height of T1. Consequently, a quasi-stationary rainband (L7) with reflectivities >50 dBZ develops over T1 and extends to the north to encompass Waipā (Fig. 12c), with individual reflectivity cores tracking northward (see footnote 2) along T1, parallel to the cloud-layer (0–10 km) mean wind vector (Fig. 8c). Long-lasting, heavy rainfall, including the storm's greatest rainfall rate, impacts Waipā during the first half of P2 (Fig. 1c).

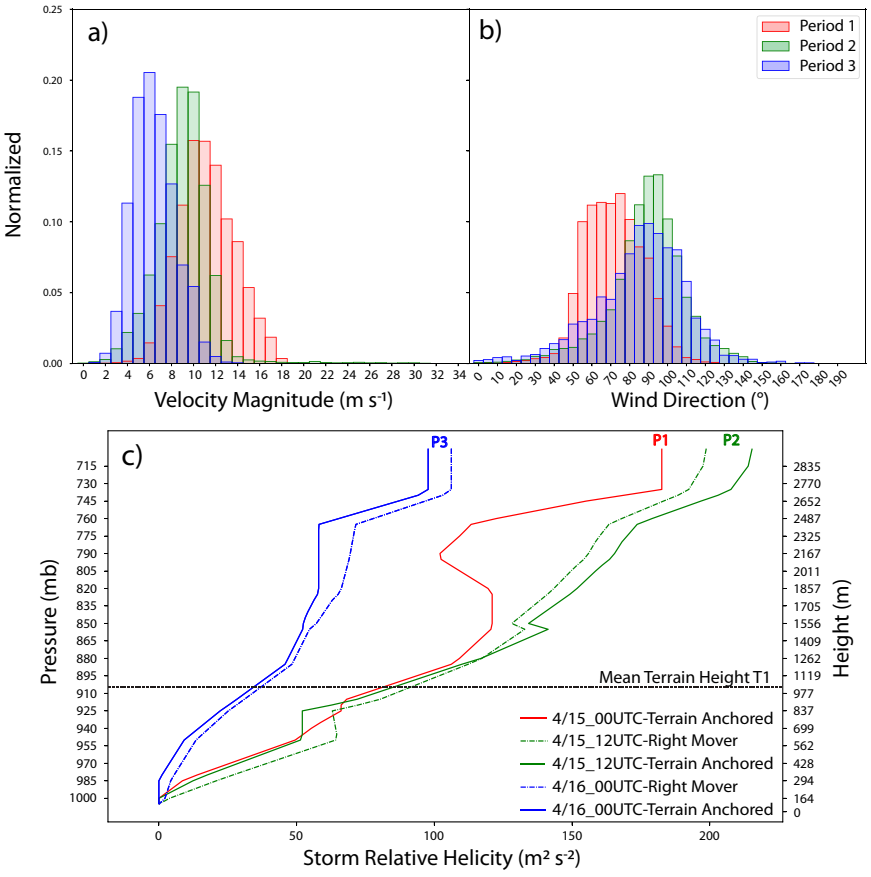

FIG. 9. (a) Histogram of the magnitude of the wind during each storm period. (b) Histogram of the wind directions during each storm period. (c) Cumulative storm-relative helicity vs height for stationary terrain-anchored storms (solid) and for right-moving storm motion (dashed) calculated using the Bunkers method (Bunkers et al. 2000) for the three storm periods. The data in (a) and (b) were calculated from PHKI Doppler radar at scan angle 2.9° using the VAD technique applied to winds below 1 km. The counts during each period were normalized by the numbers of scans during each period to allow for easier comparison.

Significant wind shear within the 0–1-km layer and veering of the winds with height by over 90° within the 0–3-km layer are evidence of SRH within the storm inflow (Fig. 8c). The 0–1- and 0–3-km terrain-anchored SRH values of 112 and 215 $m^2 s^{-2}$, respectively, are the greatest values during all periods (Fig. 9c). Radar-inferred cyclonic rotation is collocated with the areas of greatest reflectivity over T1 beginning at 1100 UTC (Fig. 12), strongly suggesting that T1 acts to reorient low-level helicity into the vertical (Fig. 9c). The developing storm circulations inferred from radar located over T1 are small (<5 km) and sporadic at first, with vertical vorticity values averaging less than 0.002 s^{-1} (Fig. 12b).

During the latter half of P2, beginning near 1300 UTC, radar velocity loops show larger and more robust midlevel circulations over T1 and T2 (see footnote 2) (latitude 22.2°, longitude from −159.5° to −159.4°) (e.g., Fig. 13). The horizontal extent of each of these circulations is up to 10 km in diameter, with peak differential velocity approaching 30 m s^{-1}. The center of the strongest cyclonic rotation is to the north of T2, and the center of anticyclonic rotation is north of T1. The radar-inferred circulations are associated with the largest reflectivity values in the vicinity of Waipā (see footnote 2). Using the same estimation for PE as in P1, another local maximum in precipitation efficiency of just over 40% is calculated using CAPE of 1886 J kg^{-1} and an average convective cloud-layer (0–10 km) wind shear of ~30 m s^{-1} (Figs. 12c and 13c).

Storm splitting is commonly initiated by the development of counterrotating pairs of vortices from the tilting of horizontal vorticity by storm updrafts and have been attributed to rainwater loading along the initial axis of the updraft (Markowski and Richardson 2010; Klemp and Wilhelmson 1978a,b). During the development of larger radar-inferred circulations near Waipā, smaller and isolated reflectivity cores with weak circulations are observed to split to the north-northwest (156°) from 1000 to 1400 UTC (Figs. 12a,b; see footnote 2). These small cores move with a velocity of 16.5 m s^{-1} and to the left of the southerly 10-km mean wind (Bunkers et al. 2000) (Fig. 8c). Higher reflectivity cores associated with stronger terrain-anchored updrafts are observed to move slowly (1.9 m s^{-1}) with a primarily westerly component

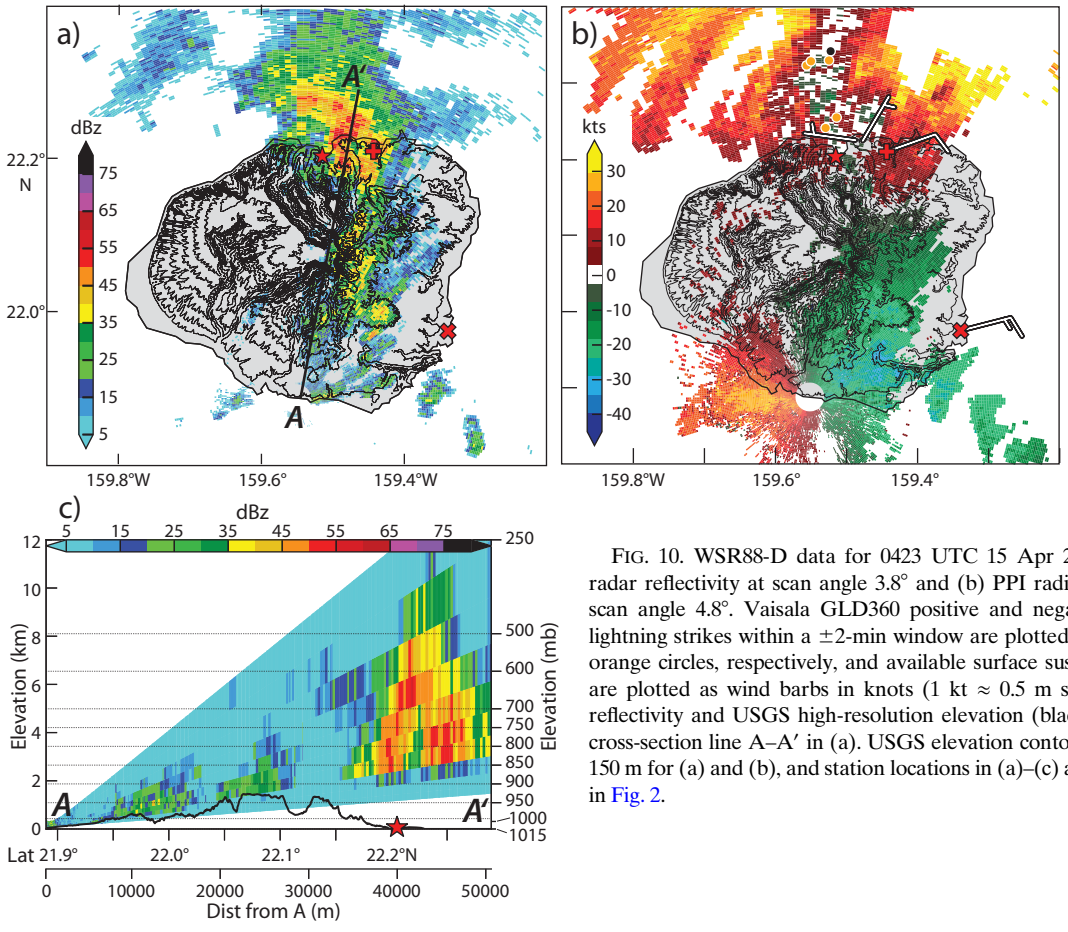

FIG. 10. WSR88-D data for 0423 UTC 15 Apr 2018. (a) PPI radar reflectivity at scan angle 3.8° and (b) PPI radial velocity at scan angle 4.8°. Vaisala GLD360 positive and negative polarity lightning strikes within a ±2-min window are plotted as black and orange circles, respectively, and available surface sustained winds are plotted as wind barbs in knots (1 kt ≈ 0.5 m s^{-1}). (c) RHI reflectivity and USGS high-resolution elevation (black line) from cross-section line A–A′ in (a). USGS elevation contours are every 150 m for (a) and (b), and station locations in (a)–(c) are as defined in Fig. 2.

to the right of the 10-km mean wind (Figs. 12a,b). Klemp and Wilhelmson (1978a,b) and Rotunno and Klemp (1982) show that in a veering wind environment, right-moving storms have a bias toward positive vertical vorticity, are self-sustaining, and contain more robust updrafts often resulting in higher reflectivity than their left-moving counterparts, as was observed in this case. Waipā is at the nexus of the storm splitting, which is a location of enhanced rainfall in supercell storms (Klemp and Wilhelmson 1978a,b; Rotunno and Klemp 1982). Radar loops show that Waipā received rain bursts from both the left-moving and right-moving cells (see footnote 2). Moreover, radar loops (see footnote 2) suggest that wind shear and terrain configuration result in persistent updrafts along T1 to the south of T2 that are separated from downdrafts on the northwest side of T2 associated with periods of torrential rainfall over Waipā.

Radar data show that the terrain-anchored line of convection starts to move eastward and gradually develops into a bow-echo squall line after 1300 UTC (Fig. 13). The radar velocity PPI (2.5–3- and 4.5–5-km elevations) show a line of enhanced convergence at the squall line's leading edge as it propagates toward the east coast of Kaua'i (Figs. 13b,d). Reflectivity data suggest that the eastward propagation is the result of a precipitation-fueled downdraft and outflow.

SRH relative to the eastward-moving squall line has values from 0 to 1 km of 79 m^2 s^{-2} and from 0 to –3 km of 200 m^2 s^{-2} comparable to the terrain-anchored SRH (Fig. 9c). The strongest mesocyclone forms just before 1500 UTC in proximity of T2 (Figs. 13b,d), with a horizontal extent of ~10 km, and the circulation is observed at every scan angle, extending beyond 3 km in depth (not shown). The maximum velocity difference is >30 ms^{-1}, corresponding to a vertical vorticity maximum of ~ 0.01 s^{-1} and lasting for over 30 min. As the bow-echo travels eastward, rainfall eventually ceases over Waipā around 1600 UTC. The bow-echo and cyclonic circulation slowly dissipate as it propagates past the east coast of Kaua'i (see footnote 2).

A peak in lightning activity is observed during the latter half of P2 with over 10 000 lightning strikes making up 65% of the total lightning strikes recorded during the storm event. The peak lightning rate occurs from 1330 to 1430 UTC, early in the development of the bow echo, with a total of 2659 strikes per hour or ~50 strikes per minute. The greatest density of lightning strikes coincided with the northern flank of the bow-echo and mesocyclone (Fig. 13b).

The axis of the greatest rainfall derived from the lightning strike density is oriented to the north-northeast and beyond the radar-inferred convective coverage of this Kauai storm

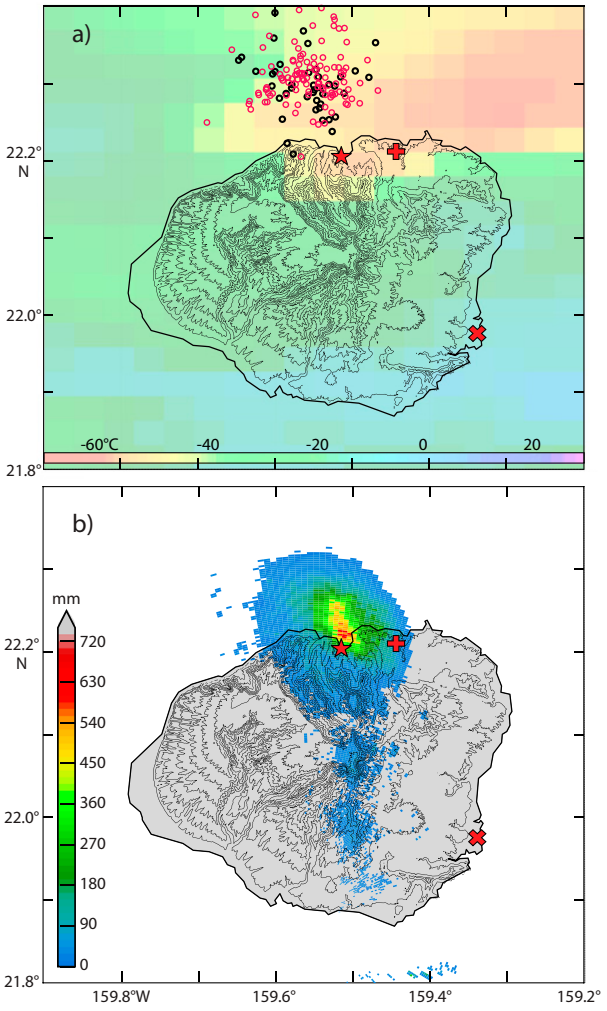

FIG. 11. (a) *GOES-15* infrared satellite imagery for 0430 UTC 15 Apr 2018 with overlay of lightning strikes for P1 (from 1900 UTC 14 Apr to 0800 UTC 15 Apr 2018) with polarity marked as in Fig. 10. (b) Rainfall accumulation derived from WSR88-D at scan angle 4.9° during P1. USGS elevation contours are every 150 m; Waipā, Princeville, and Lihue stations are marked as in Fig. 2.

(Fig. 14b). The lightning density aligns in the direction of the winds at the freezing level, the EL (Fig. 7c) as well as in alignment with envelope of coldest cloud-top temperatures (not shown, but similar to Fig. 11a). The close alignment and extension of lightning density with the coldest cloud-top temperatures suggests the convective cores were strong enough to reach above the freezing level, produce a mixed phase region, and become strongly advected by the upper-level winds away from the islands. These observations support the presence of strong and deep layer environmental shear and favorable storm ventilation during P2.

Two distinct zones of greater rainfall accumulation occurred during P2. A primary maximum of >600 mm is located over the terrain T1 and extends NNE in the close proximity to Waipā (Fig. 14a). The NNW storm splitting contributes to the rainfall total over Waipā during this period. It is suggested that wind shear at levels below available radar scans accounts for the offset between the location of maximum rainfall and Waipā. A second region of enhanced rainfall that extends from north central Kaua'i southeastward is associated with the propagating bow echo (Fig. 14a).

c. Period 3: 1800 UTC 15 April–0400 UTC 16 April

A partial sounding ending at 300 hPa shows similar saturation and conditional instability as during P2 (Fig. 7d). Slightly warmer surface temperatures and dewpoints at the surface result in the highest CAPE = 1921 J kg^{-1} for all three periods. The 0–1-km winds exhibit similar veering with height as during P2 but are less strong in magnitude (Fig. 8d). A near-critical Froude number of 0.98 is calculated for the mean terrain height of T1, which again supports terrain-anchored convection along T1.

VAD analysis for P3 shows a decrease in storm-relative wind velocity when compared with P1 and P2 (Fig. 9a). The storm-relative wind direction distribution is primarily easterly, similar to P2, which favors similar orographic convective initiation along T1 (Fig. 9b). The diminished magnitude of the low-level winds results in a reduction in terrain-anchored SRH values (0–1 km = 49 m^2 s^{-2}; 0–3 km = 135 m^2 s^{-2}) (Fig. 9c).

A 5-km-wide rainband (40–60 dB*Z*) develops (see footnote 2) along and to the north of T1 beginning at 2000 UTC, and by 2100 UTC the rainband doubles in width, extending to encompass T2 and Waipā (Fig. 15a). Reflectivity cores extend only to 8 km in height and encompass less area in the horizontal plane relative to P2, consistent with weaker low-level winds (Fig. 15c).

Anticyclonic and cyclonic circulation pairs develop on the northern end of the rainband (Fig. 15b). Similar to P2, the anticyclonic rotation is on the left and just east of Waipā and the cyclonic rotation is north of T2. From 2100 to 2300 UTC, the rainband maintains its spatial extent and slowly moves eastward. This marks the end of the 24-h rainfall record for Waipā, which occurred 2 h after the onset of terrain-anchored convection (Fig. 1c; see footnote 2). Consistent with the reduced SRH during P3, the radar-inferred circulations are less well defined and more sporadic with maximum differential velocity of 20 m s^{-1} (Fig. 9). Radar analysis beyond the 24-h rainfall record period, starting at 2200 UTC, shows a bow echo with a weak convergence line and smaller-diameter radar-inferred circulation than during P2 (not shown).

Observations suggest that enhanced lightning frequency and strike locations coincide with enhanced radar reflectivity and inferred circulations (Fig. 15). The majority of the cloud-to-ground lightning strikes were negative (80%) during P3, consistent with previously documented rates in high precipitating supercell environments (Fig. 15b) (Branick and Doswell 1992; Knapp 1994).

Spatial patterns of lightning density are in general agreement with the radar-derived rainfall pattern (Fig. 16). An estimated PE of 33%, smallest for all periods, is found using a CAPE of 1921 J kg^{-1} and an average convective cloud-layer (0–8 km) shear of 20 m s^{-1}. Rainfall totals for P3 show that the majority of rainfall accumulation occurs east of T1 and southeast of T2 (Fig. 16).

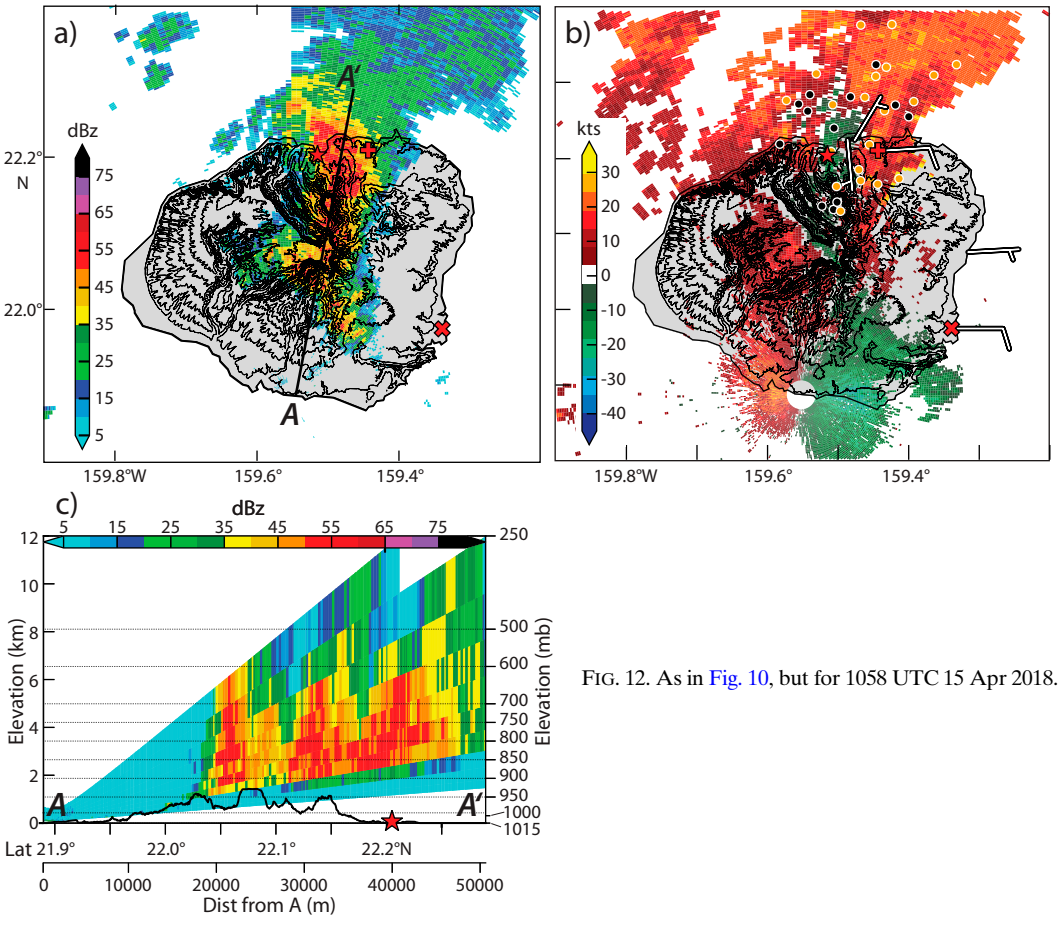

FIG. 12. As in Fig. 10, but for 1058 UTC 15 Apr 2018.

d. Analysis of the record rainfall accumulation: 2245 UTC 14 April–2245 UTC 15 April

In this section, total 24-h rainfall accumulation patterns estimated from radar reflectivity, specific differential phase, and lightning density fields are analyzed spatially and temporally and compared with rain gauge accumulation data to gain further insight into the record-setting rain event of 14–15 April 2018.

The greatest rainfall accumulation, as documented by the radar reflectivity, is located over the ridge and the east-facing slopes of T1 (Figs. 4 and 17a). The maximum rainfall accumulation north of T1 is associated with advection of terrain-anchored precipitation cores northward by the mean midlevel winds and precipitation associated with recurring mesoscale circulations just to the North of T1. The radar-derived rainfall accumulation for the 24-h period for Waipā is ~700 mm. However, the peak accumulation of 1232 mm was located 2.2 km east-southeast of Waipā (Fig. 18, inset). The location error was primarily the result of drift in rainfall imparted by strong winds below ~2.5 km over Waipā, below which the radar beam is blocked by terrain and radar analysis is impaired.

The average rainfall rate for each period was ~70 mm h^{-1}. The average raindrop diameter for orographic rainfall in Hawaii of ~70 mm h^{-1} is ~2 mm (Blanchard 1953). The radar scan angle is limited by terrain to above ~2.5-km elevation over Waipā. Using wind data from the Lihue sounding and a terminal velocity of ~6 m s^{-1} for the average droplet size (Foote and Du Toit 1969) to estimate the mean droplet advection, brings the location of maximum rainfall to within 1 km of Waipā. While reflectivity-derived rainfall totals demonstrate good accuracy in comparison with the 24-h Waipā total, rain rates during P1 are underestimated while those during P2 and P3 are overestimated and the location of the maximum is too far to the east (Fig. 18, inset).

The K_{DP} method proved to be the most accurate way to estimate rainfall rates; K_{DP} matched the rain gauge observed rainfall rates pretty closely during P1 and P3 and only slightly overestimated them during the peak hours of P2 (Fig. 18). The K_{DP} spatial accumulation map provides the best agreement with the rain gauge data, with greater rainfall totals north of T1, and extending closer to Waipā than the reflectivity-based estimate (Figs. 17a,b). The K_{DP} estimates more than 1100 mm of rainfall accumulation at Waipā (Fig. 17b), a big improvement over the 700-mm estimate from reflectivity. With the K_{DP} method, there was no need to apply a wind drift correction because of K_{DP}'s greater spatial accuracy in high-wind-shear environments (Kumjian and Ryzhkov 2009).

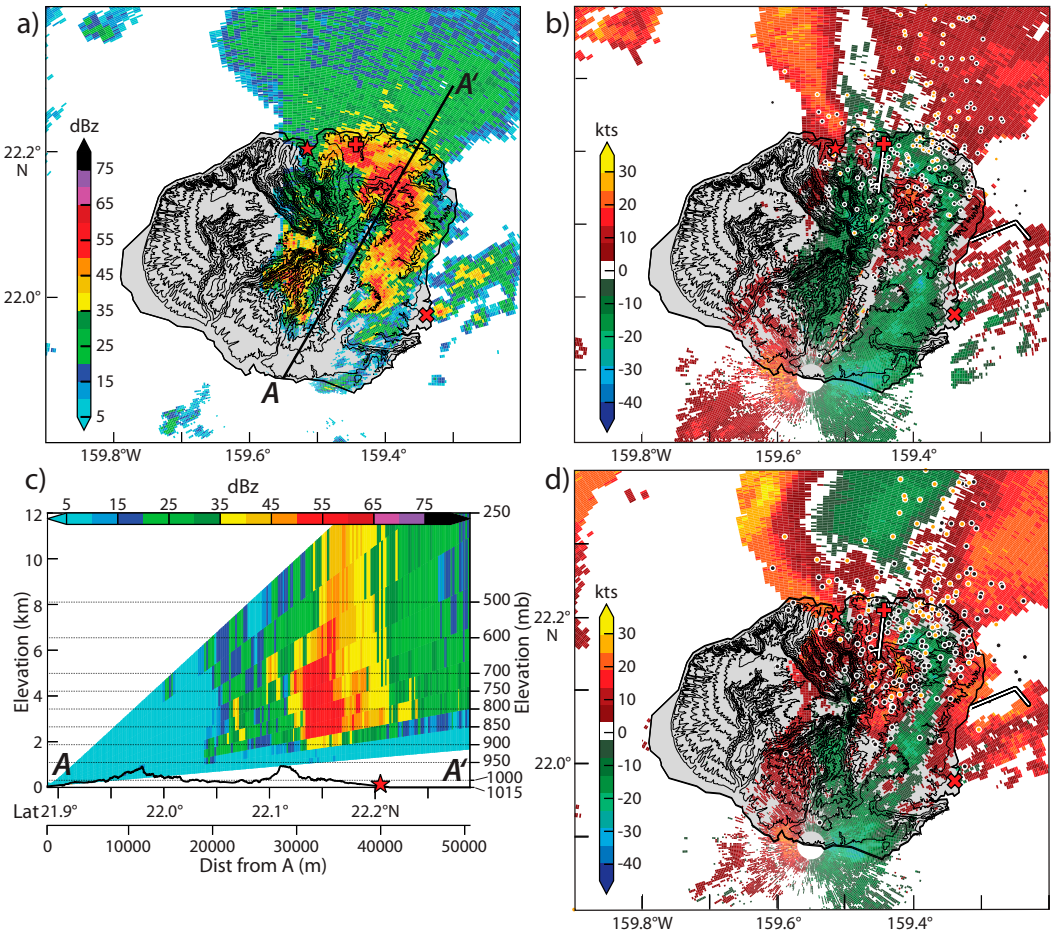

FIG. 13. As in Fig. 10, but for 1456 UTC 15 Apr, and (d) with the addition of the radial velocity image for scan angle 6.2°.

Rainfall rates were derived from GLD360 lightning data by using the stroke -versus-reflectivity relationship developed over the northwestern Pacific Ocean by Stolz et al. (2014) and then applying the Rosenfeld tropical Z–R relationship. The lightning-rainfall method is not affected by terrain blocking of the radar signal and provides an independent approach to computing rainfall rates. Just under 14 000 lighting strikes occurred within this 24-h record period; lightning strikes during P1 account for just 14% of the total. The lingering presence of the subtropical high and inversion layer inhibited deep convection and the formation of a mixed-phase layer during P1 (Fig. 7a). Consequently, the lightning derived rainfall accumulation map underestimates the rainfall totals received at Waipā by ~75% (Fig. 17c) due to the infrequency of lightning during P1 (Fig. 11a). Cumulatively, the lightning-rainfall estimation results in a little over 300 mm over Waipā over the 24-h record period (Fig. 18). The rainfall accumulation map shows nonuniform rainfall totals. The pattern of maxima is oriented to the NNE (Fig. 17c), in agreement with the mean wind vector in the mixed-phase layer during P2 and P3 (Figs. 8b–d). When a wind drift correction is applied, using this wind vector, the lightning derived rainfall accumulation maxima (~500 mm) falls 3.5 km north-northeast of Waipā and over the water, proving to be the least accurate method of estimating rainfall accumulation for this storm. This is not surprising because the lightning-derived rainfall targets rainfall from deep convective clouds that contain active mixed-phase regions and is unable to capture rain from warm rain nor stratiform rain processes.

5. Conclusions and discussion

This case study examines a series of three distinct periods of thunderstorm activity over the central and eastern topography of Kaua‘i, resulting in over 30 h of rainfall that caused flash flooding and historic flood damage and set a new 24-h U.S. rainfall record at the Waipā Garden rain gauge located on the north coast of Kaua‘i.

a. Conclusions

- On the synoptic scale, positive vorticity and cold-air advection aloft produced an inverted trough at the surface that enhanced convergence and lifting through Ekman pumping which helped to moisten midlevels and promote destabilization (Fig. 19).

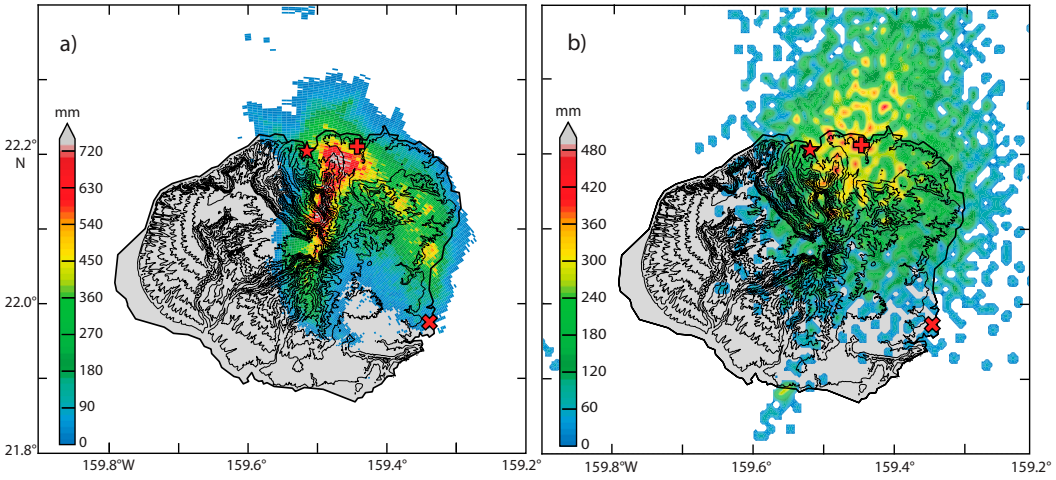

FIG. 14. (a) Rainfall accumulation derived from WSR-88D at scan angle 4.9° during P2, and (b) rainfall accumulation derived from Vaisala GLD360 accumulated lightning density (strikes per kilometer squared) during P2. USGS elevation contours areevery 150 m; Waipā, Princeville, and Lihue stations are marked as in Fig. 2.

- Persistent northeasterly and then easterly low-level flow resulted in orographic lifting across Kaua'i's northeast- and east-facing slopes, which triggered terrain-anchored convective storms (Fig. 20a).
- Doppler radar and sounding data confirm that the terrain relative flow below 1 km exceeded 10 m s^{-1}, which is a necessary condition for supercell development.

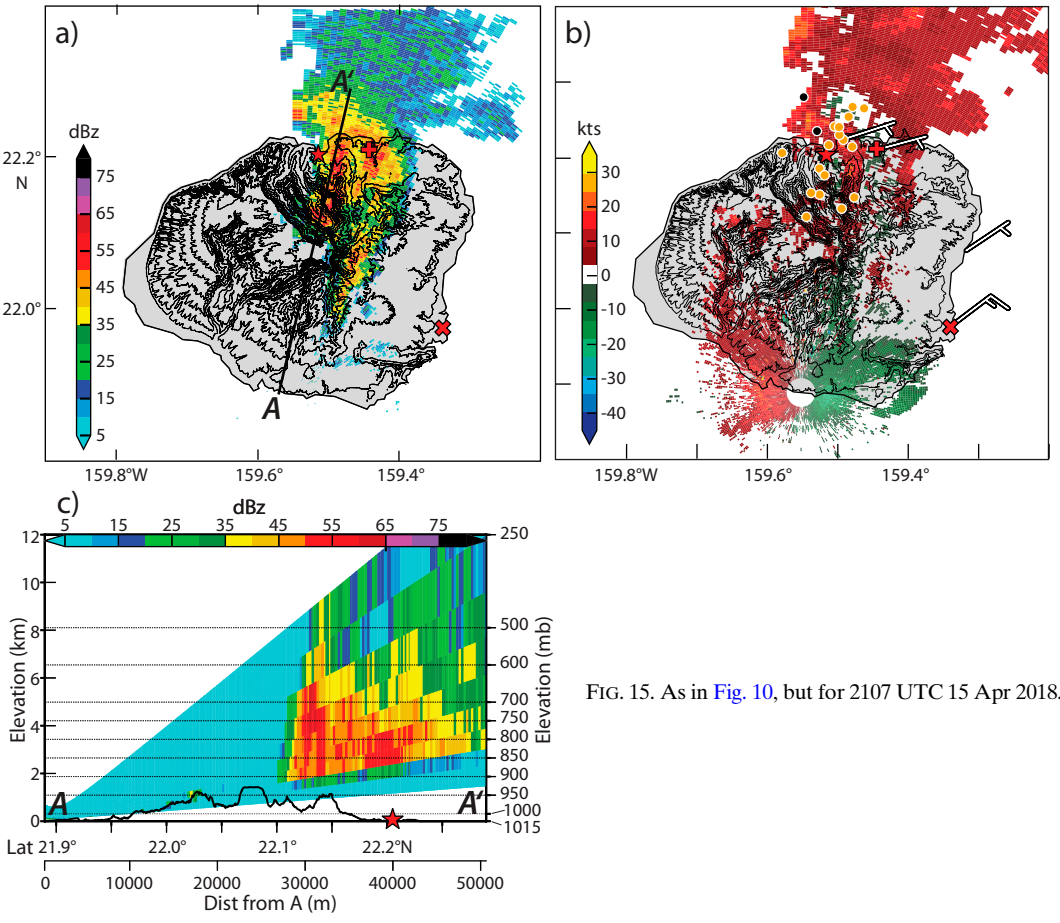

FIG. 15. As in Fig. 10, but for 2107 UTC 15 Apr 2018.

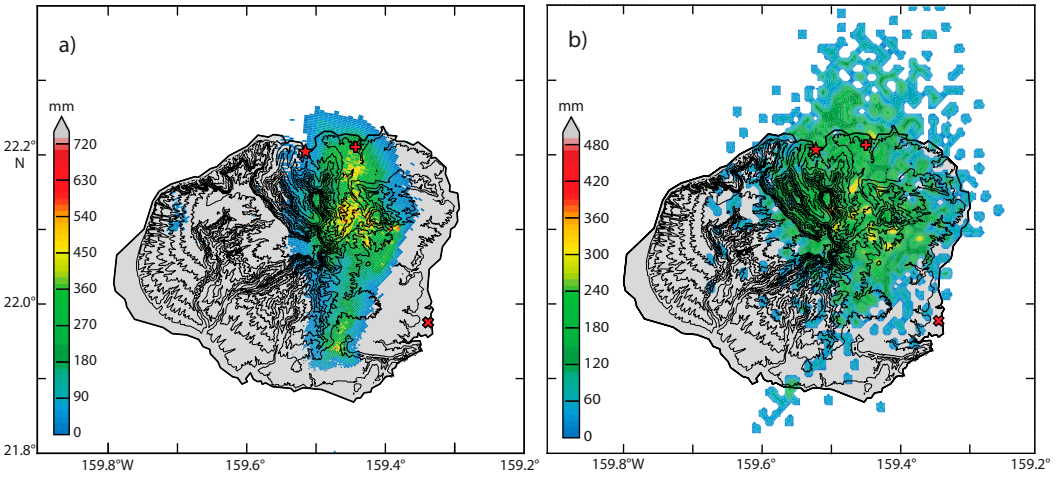

FIG. 16. As in Fig. 14, but during P3.

- Strong directional wind shear within the storm inflow layer created large storm-relative helicity or streamwise vorticity, which are well correlated with storm rotation and the development of supercells (Fig. 20b).
- Radial velocity couplets in the radar data suggest that locations where streamwise vorticity is redirected into the vertical becomes a source of mesoscale circulation over Kaua'i's steep terrain (e.g., Figs. 9 and 13).

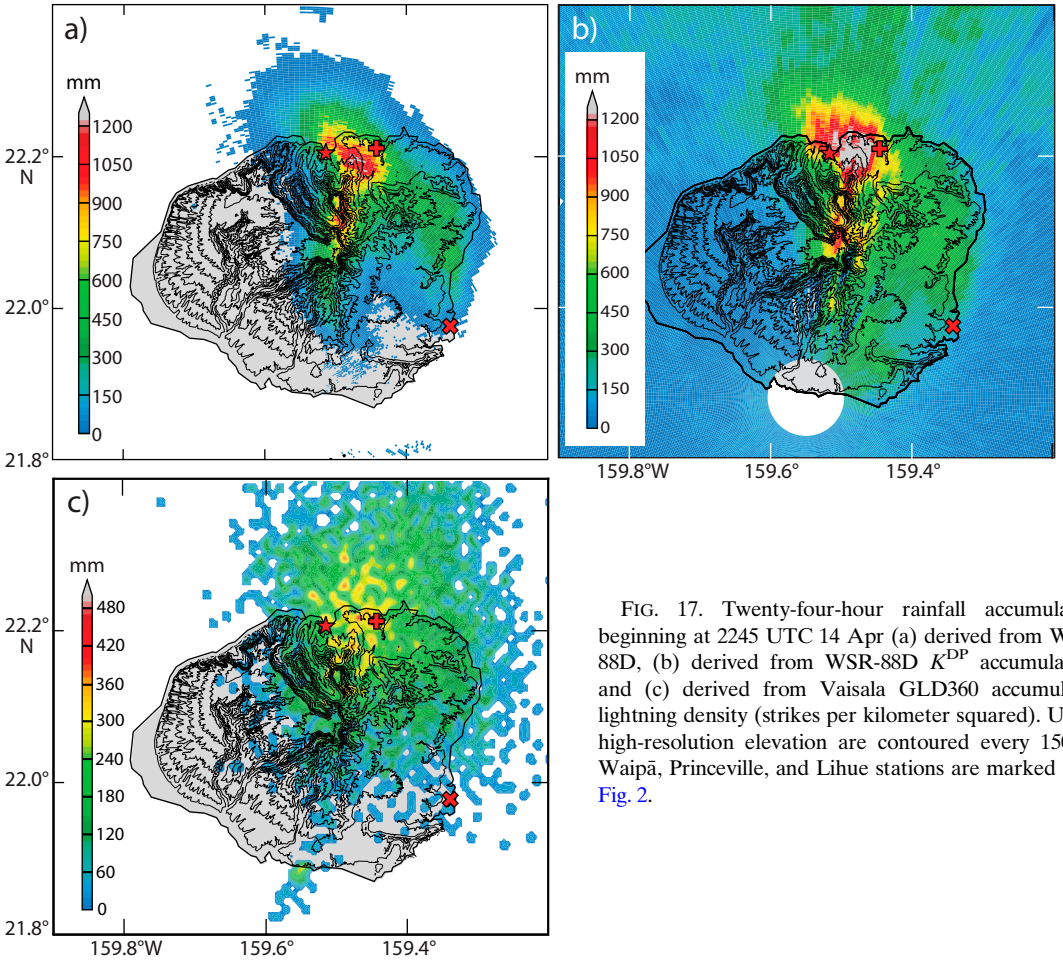

FIG. 17. Twenty-four-hour rainfall accumulation beginning at 2245 UTC 14 Apr (a) derived from WSR-88D, (b) derived from WSR-88D K^{DP} accumulation, and (c) derived from Vaisala GLD360 accumulated lightning density (strikes per kilometer squared). USGS high-resolution elevation are contoured every 150 m. Waipā, Princeville, and Lihue stations are marked as in Fig. 2.

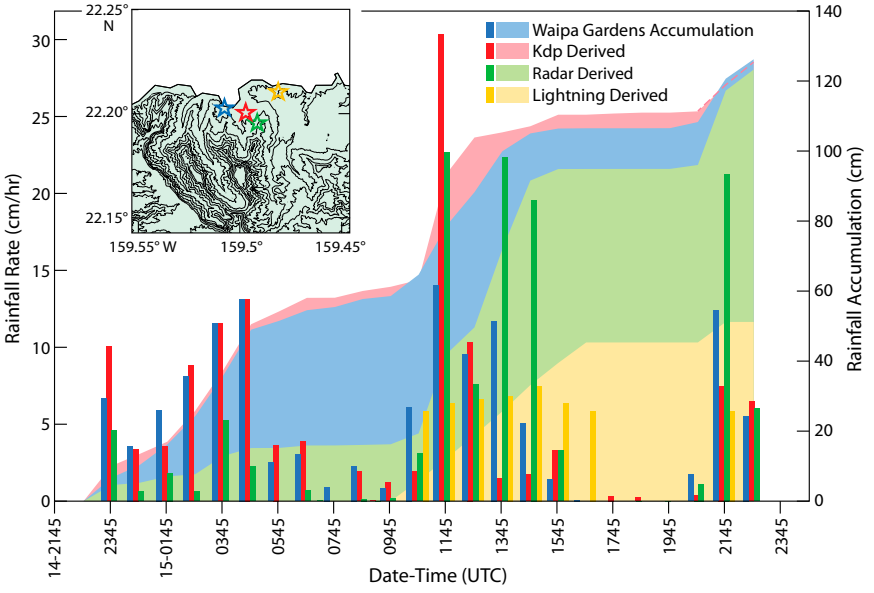

FIG. 18. Time series for the maximum precipitation over Kaua'i using each method of estimating rainfall rate (histogram) and rainfall accumulation (shaded) that is described in Fig. 17. Inset: Locations of maximum rainfall accumulation plotted for each method with no wind drift corrections applied.

- Radar velocity loops (see footnote 2) suggest that terrain induced circulations combined with deep layer mean southerly shear are linked to the development of a persistent mesocyclone to the north of T1 that contributed to the rainfall accumulation at Waipā (Fig. 20a).

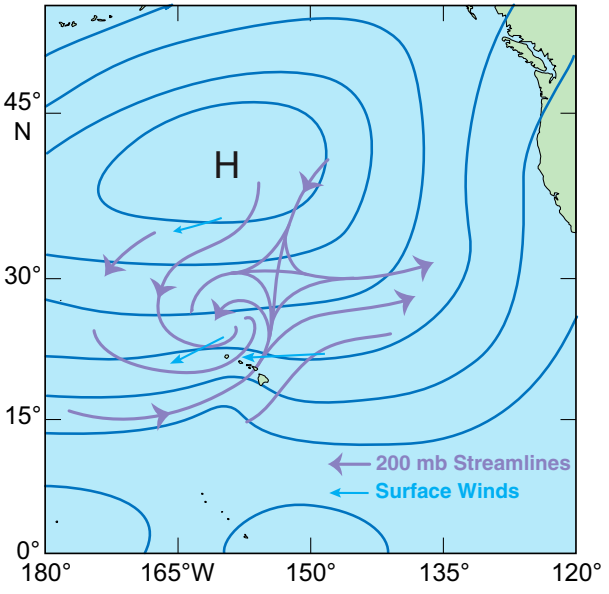

FIG. 19. Conceptual diagram showing an upper-level trough approaching from the northwest, inducing an inverted trough at the surface over Hawaii. Purple contours are 200-hPa streamlines, dark-blue contours are isobars, and light-blue arrows indicate surface wind vectors.

- Radar observations suggest that windshear and terrain configuration result in persistent updrafts along T1 to the south of T2 that are separated from downdrafts on the northwest side of T2 associated with periods of torrential rainfall over Waipā (Figs. 17 and 20a).
- Radar analysis provides evidence that multiple rounds of storm cell splitting occurred to the north of T1 as a result of very heavy rain bursts that are a hallmark of supercell thunderstorms.
- The eastward-propagating echoes during P2 develop into a well-defined bow echo pattern with a mesocyclone on its northern flank (Fig. 13).
- Toward the end of P2 and P3, terrain-anchored reflectivity cores transition to right-moving echoes that propagate eastward away from Waipā, signaling the end of heavy rainfall over Waipā by preventing low-level inflow from reaching the terrain.
- Rainfall accumulation over Kaua'i derived from the specific differential phase demonstrated the best temporal and spatial accuracy when compared with reflectivity derived and lightning derived rainfall and the rain gauge rainfall total at Waipā.

b. Discussion

The acceleration of the easterly component of the winds around the 1-km level, seen in rawinsonde and radar data during the event, may be evidence of an ageostrophic low-level jet (LLJ) tied to quasigeostrophic forcing from the jet streak pattern aloft (Uccellini and Johnson 1979). LLJs also enhance moisture transport, warm-air advection, and convergence with rising motion within their exit regions, all of which increase the tendency of heavy precipitation, especially at night (Bonner 1966; Maddox and Doswell 1982; Whiteman

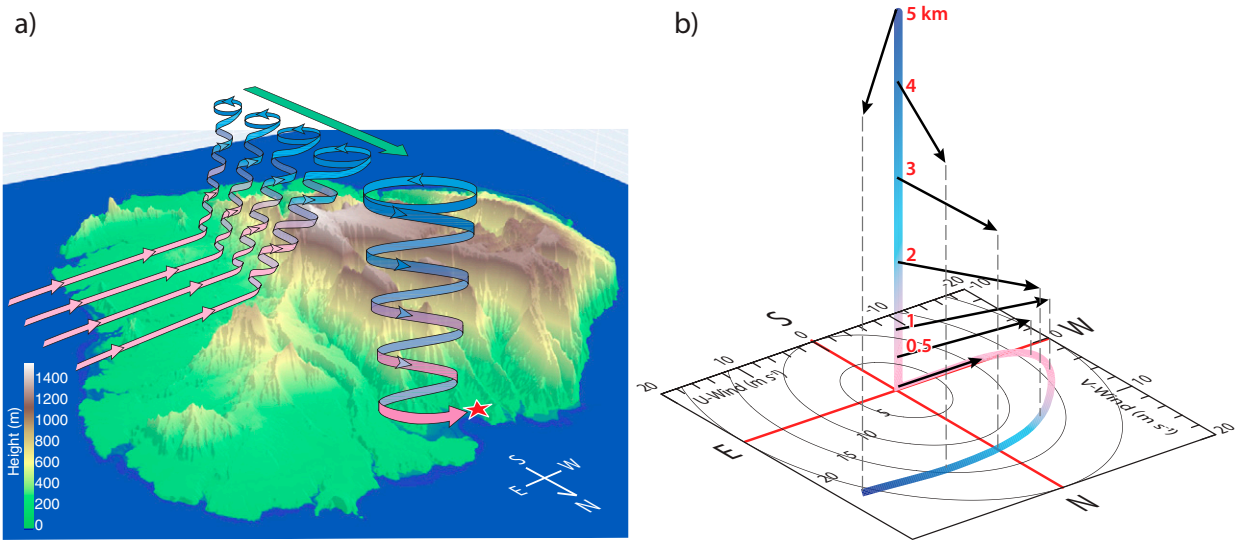

FIG. 20. (a) A 3D schematic during the peak rainfall of the Kaua'i event viewed from the northeast. The vector winds are color coded with increasing height from pink to blue. Vector winds (pink) entering from the east represent sheared low-level helical inflow lifted by the east slopes of Mount Wai'ale'ale (T1) triggering deep convection with rotating updrafts. Cloud-layer (0–10 km) mean wind (green vector at the top) from the south is parallel to the terrain gradient of T1 and acts to advect cyclonic circulations and precipitation particles within the updrafts northward. Aggregation of these rotating updrafts along the terrain boundary leads to the upscale development of the observed mesocyclone, with precipitation-driven sinking motion to the north of T1 and T2 and torrential rains over Waipā (red star). Refer to Fig. 2 for locations of terrain features T1 and T2. (b) Conceptual hodograph based on Fig. 8c, illustrating the magnitude of the shear of the horizontal winds in the lowest 5 km of the atmosphere, with easterly winds in the lowest levels veering to southerly at midlevels. The vertical axis and hodograph are color coded with increasing height from pink to blue. Black vectors denote direction and magnitude of the winds at the indicated heights.

et al. 1997). The evidence suggests that the strength of the low-level mean winds orthogonal to the terrain and the magnitude of the low-level wind shear in the storm inflow layer (Fig. 8) are responsible for the observed increase in the size and magnitude of terrain-anchored convection, especially at night during P2 (see footnote 2) (Figs. 12 and 13).

Strong low-level vertical wind shear favors stronger and wider convective updrafts, greater cold pools, and more precipitation production (Warren et al. 2017). LLJs have also been linked to the presence of boundary layer rolls attributed to low-level inflection point instability, evidence for which was observed during the peak convection for this storm event (Figs. 7 and 13b) (Raymond 1978; Brown 1980; Bryan et al. 2007) and are consistent with the observed strong SRH (Fig. 9c).

Small differences in the magnitude and direction of the low-level mean winds relative to the terrain features of Kaua'i proved fundamental to the recurrence and persistence of the thunderstorms and the magnitude of rainfall that impacted Kaua'i and Waipā (Figs. 4 and 9a,b). Radar data suggest that terrain elements T1 and T2 act as physical barriers that prevent the stable cold pool outflow, which was created from the heavy rain extending north of T1, from interfering with the inflow south of T2 (Figs. 4 and 17). A case study of convective upscale growth of supercells into mesoscale convective complexes in South America concluded that terrain blocking could lead to cold-pool segregation from the storm updrafts and the development of deeper cold pools. Terrain blocking also indirectly influences the surrounding wind shear and CAPE, favoring upscale convective growth and supercell longevity in the lee of terrain (Mulholland et al. 2019; Markowski and Dotzek 2011).

The strength of the veering in the boundary layer below the level of Kaua'i's mountain summits combined with the alignment of the lower-level east winds orthogonal to the slopes of Kaua'i's terrain resulted in enhanced rotation in the radar data, a unique aspect of this case. Streamwise vorticity, approaching 100 m^2 s^{-2} below Kauai'i's mountain summits (~1.5 km) during P2 and P3, are comparable to those in environments that support supercells in the central plains (Fig. 9c). In contrast to a supercell in the central U.S. plains, where the gust front provides the lifting mechanism, in this event the orography provided the lifting mechanism (Fig. 20). Because the terrain is stationary there is continual regeneration of the rotating updrafts so long as the inflow is characterized by strong streamwise vorticity.

A study by Dial et al. (2010) concluded that upscale convective initiation along synoptic-scale airmass boundaries increased when the low-level winds were perpendicular to this boundary and when the cloud-layer mean wind shear was aligned nearly parallel to the boundary. Observations in this case show similar dynamics with the low-level winds oriented perpendicular to the main terrain axis of T1 and the deep layer mean winds oriented parallel to T1 (Fig. 20). These circumstances favor the tilting and stretching of existing vorticity within orographic updrafts spinning up and increasing the

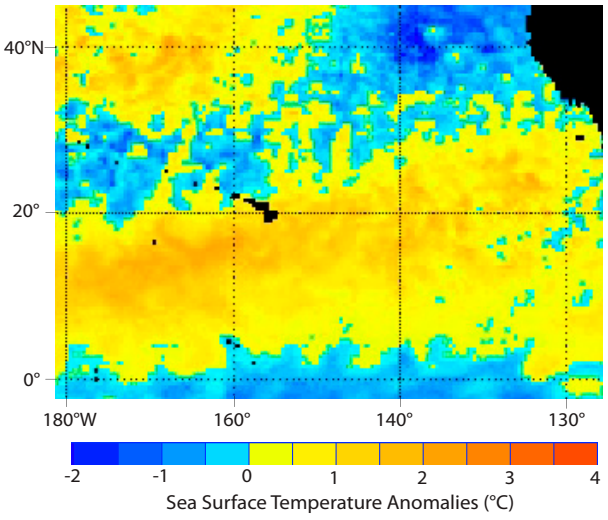

FIG. 21. Sea surface temperature anomalies (°C) for 16 Apr 2018 from NOAA's Office of Satellite and Product Operations. The resolution of the data is 50 km.

vertical vorticity. We speculate that the convergence and aggregation of these vortical updrafts along the terrain over time led to the upscale development of observed mesocyclones (Figs. 12 and 20). This mechanism of vertical vorticity aggregation via mergers of vortical updrafts has been well documented in the genesis of high precipitating supercells (Lemon 1976; Barnes 1978; Kulie and Lin 1998; Finley et al. 2001).

Upshear forces associated with vertical pressure perturbations help maintain surface-based convection during otherwise stable early morning environments (Coffer and Parker 2015). Forcing from vertical pressure perturbations produce greater vertical motion, lower lifted condensation level height, increased intake of non-buoyant and high CAPE parcels (Nielsen and Schumacher 2018). Downshear forcing from vertical pressure perturbations favors greater downward motion (Markowski and Richardson 2010). In the Kaua'i case, these vertical pressure perturbation forces associated with the mesocyclone act to increase moisture and SRH within the updrafts on the upshear (south) side of the mesocyclone and support convective initiation and updraft rotation. With the aid of the terrain boundary of T1 and T2, the pressure perturbation forces on the downshear (north) side of the mesocyclone are conducive to updraft/downdraft separation, promoting persistent heavy rainfall to the north of T1 and T2 in the vicinity of Waipā.

The varied mesoscale structures seen in extreme Hawaiian rainfall events (Murphy and Businger 2011; Lyman et al. 2005; Kodama and Barnes 1997) and their potential for destructive impacts underscore the need for continued research. The synoptic pattern common to events like this one produced an inverted surface trough, which resulted in easterly surface flow that passed over anomalous SST temperatures as much as 2°C above the climatological average (Fig. 21). As sea surface temperatures continue to rise, marine boundary layer moisture grows exponentially, and rainfall events with a similar synoptic pattern are destined to become more extreme (Fig. 19; Caruso and Businger 2006). Work is currently under way on an analytical analysis of the impact of terrain on vertical vorticity generation for various environmental shears and orographic configurations. This effort is paired with an investigation using an idealized convective cloud model of mesocyclone formation forced by terrain, with a focus on the linear and nonlinear dynamic pressure perturbations associated with storm rotation. In addition, the effects of helical inflow impacting different mountain geometries and aspect ratios will be studied to understand which conditions foster the greatest redirection of streamwise vorticity into vertical vorticity, as well as which conditions foster the greatest potential for aggregation and upscale growth into supercells.

Acknowledgments. We are grateful for the graphics support from Nancy Hulbirt. Doctor Giuseppe Torri provided valuable insights into the dynamics of severe storms. Thanks are given to Kevin Kodama for rainfall data and discussions about the event. We are very grateful for the thoughtful and constructive reviews provided by John M. Peters of Naval Postgraduate School and two anonymous reviewers. This research was supported by the Office of Naval Research under ONR Award N00014-18-1-2166 and by the Johnathan Merage Foundation.

REFERENCES

Akaeda, K., J. Reisner, and D. Parsons, 1995: The role of mesoscale and topographically induced circulations in initiating a flash flood observed during the TAMEX project. *Mon. Wea. Rev.*, **123**, 1720–1739, https://doi.org/10.1175/1520-0493(1995)123<1720:TROMAT>2.0.CO;2.

Alpers, W., and B. Brümmer, 1994: Atmospheric boundary layer rolls observed by the synthetic aperture radar aboard the ERS-1 satellite. *J. Geophys. Res.*, **99**, 12 613–12 621, https://doi.org/10.1029/94JC00421.

Barnes, S. L., 1978: Oklahoma thunderstorms on 29–30 April 1970: Part I: Morphology of a tornadic storm. *Mon. Wea. Rev.*, **106**, 673–684, https://doi.org/10.1175/1520-0493(1978)106<0673:OTOAPI>2.0.CO;2.

Blanchard, D. C., 1953: Raindrop size-distribution in Hawaiian rains. *J. Meteor.*, **10**, 457–473, https://doi.org/10.1175/1520-0469(1953)010<0457:RSDIHR>2.0.CO;2.

Bonner, S. F., 1966: Lucan and the declamation schools. *Amer. J. Philol.*, **87**, 257–289, https://doi.org/10.2307/292851.

Bonner, W. D., 1968: Climatology of the low level jet. *Mon. Wea. Rev.*, **96**, 833–850, https://doi.org/10.1175/1520-0493(1968)096<0833:COTLLJ>2.0.CO;2.

Brandes, E. A., A. V. Ryzhkov, and D. S. Zrnić, 2001: An evaluation of radar rainfall estimates from specific differential phase. *J. Atmos. Oceanic Technol.*, **18**, 363–375, https://doi.org/10.1175/1520-0426(2001)018<0363:AEORRE>2.0.CO;2.

Branick, M. L., and C. A. Doswell III, 1992: An observation of the relationship between supercell structure and lightning ground-strike polarity. *Wea. Forecasting*, **7**, 143–149, https://doi.org/10.1175/1520-0434(1992)007<0143:AOOTRB>2.0.CO;2.

Brown, R. A., 1980: Longitudinal instabilities and secondary flows in the planetary boundary layer: A review. *Rev. Geophys. Space Phys.*, **18**, 683–697, https://doi.org/10.1029/RG018i003p00683.

Bryan, G. H., R. Rotunno, and J. M. Fritsch, 2007: Roll circulations in the convective region of a simulated squall line. *J. Atmos. Sci.*, **64**, 1249–1266, https://doi.org/10.1175/JAS3899.1.

Bunkers, M. J., B. A. Klimowski, J. W. Zeitler, R. L. Thompson, and M. L. Weisman, 2000: Predicting supercell motion using a new hodograph technique. *Wea. Forecasting*, **15**, 61–79, https://doi.org/10.1175/1520-0434(2000)015<0061:PSMUAN>2.0.CO;2.

Businger, S., T. Birchard Jr., K. R. Kodama, P. A. Jendrowski, and J.-J. Wang, 1998: A bow echo and severe weather associated with a kona low in Hawaii. *Wea. Forecasting*, **13**, 576–591, https://doi.org/10.1175/1520-0434(1998)013<0576:ABEASW>2.0.CO;2.

Cao, G., T. W. Giambelluca, D. E. Stevens, and T. A. Schroeder, 2007: Inversion variability in the Hawaiian trade wind regime. *J. Climate*, **20**, 1145–1160, https://doi.org/10.1175/JCLI4033.1.

Caruso, S. J., and S. Businger, 2006: Subtropical cyclogenesis over the central North Pacific. *Wea. Forecasting*, **21**, 193–205, https://doi.org/10.1175/WAF914.1.

Coffer, B. E., and M. D. Parker, 2015: Impacts of increasing low-level shear on supercells during the early evening transition. *Mon. Wea. Rev.*, **143**, 1945–1969, https://doi.org/10.1175/MWR-D-14-00328.1.

——, ——, R. L. Thompson, B. T. Smith, and R. E. Jewell, 2019: Using near-ground storm relative helicity in supercell tornado forecasting. *Wea. Forecasting*, **34**, 1417–1435, https://doi.org/10.1175/WAF-D-19-0115.1.

Davies-Jones, R., 1984: Streamwise vorticity: The origin of updraft rotation in supercell storms. *J. Atmos. Sci.*, **41**, 2991–3006, https://doi.org/10.1175/1520-0469(1984)041<2991:SVTOOU>2.0.CO;2.

Dial, G. L., J. P. Racy, and R. L. Thompson, 2010: Short-term convective mode evolution along synoptic boundaries. *Wea. Forecasting*, **25**, 1430–1446, https://doi.org/10.1175/2010WAF2222315.1.

Droegemeier, K. K., S. M. Lazarus, and R. Davies-Jones, 1993: The influence of helicity on numerically simulated convective storms. *Mon. Wea. Rev.*, **121**, 2005–2029, https://doi.org/10.1175/1520-0493(1993)121<2005:TIOHON>2.0.CO;2.

Finley, C. A., W. R. Cotton, and R. A. Pielke Sr., 2001: Numerical simulation of tornadogenesis in a high-precipitation supercell. Part I: Storm evolution and transition into a bow echo. *J. Atmos. Sci.*, **58**, 1597–1629, https://doi.org/10.1175/1520-0469(2001)058<1597:NSOTIA>2.0.CO;2.

Foote, G. B., and P. S. Du Toit, 1969: Terminal velocity of raindrops aloft. *J. Appl. Meteor.*, **8**, 249–253, https://doi.org/10.1175/1520-0450(1969)008<0249:TVORA>2.0.CO;2.

Foster, J., and M. Bevis, 2003: Lognormal distribution of precipitable water in Hawaii. *Geochem. Geophys. Geosyst.*, **4**, 1065, https://doi.org/10.1029/2002GC000478.

——, ——, Y. L. Chen, S. Businger, and Y. Zhang, 2003: The Ka'u storm (November 2000): Imaging precipitable water using GPS. *J. Geophys. Res.*, **108**, 4585, https://doi.org/10.1029/2003JD003413.

James, R. P., and P. M. Markowski, 2010: A numerical investigation of the effects of dry air aloft on deep convection. *Mon. Wea. Rev.*, **138**, 140–161, https://doi.org/10.1175/2009MWR3018.1.

Klemp, J. B., and R. B. Wilhelmson, 1978a: Simulations of right- and left-moving storms produced through storm splitting. *J. Atmos. Sci.*, **35**, 1097–1110, https://doi.org/10.1175/1520-0469(1978)035<1097:SORALM>2.0.CO;2.

——, and ——, 1978b: The simulation of three-dimensional convective storm dynamics. *J. Atmos. Sci.*, **35**, 1070–1096, https://doi.org/10.1175/1520-0469(1978)035<1070:TSOTDC>2.0.CO;2.

Knapp, D. I., 1994: Using cloud-to-ground lightning data to identify tornadic thunderstorm signatures and nowcast severe weather. *Natl. Wea. Dig.*, **19**, 35–42.

Kodama, K. R., and G. M. Barnes, 1997: Heavy rain events over the south-facing slopes of Hawaii: Attendant conditions. *Wea. Forecasting*, **12**, 347–367, https://doi.org/10.1175/1520-0434(1997)012<0347:HREOTS>2.0.CO;2.

——, and S. Businger, 1998: Weather and forecasting challenges in the Pacific region of the National Weather Service. *Wea. Forecasting*, **13**, 523–546, https://doi.org/10.1175/1520-0434(1998)013<0523:WAFCIT>2.0.CO;2.

Kulie, M. S., and Y. L. Lin, 1998: The structure and evolution of a numerically simulated high-precipitation supercell thunderstorm. *Mon. Wea. Rev.*, **126**, 2090–2116, https://doi.org/10.1175/1520-0493(1998)126<2090:TSAEOA>2.0.CO;2.

Kumjian, M. R., 2013: Principles and applications of dual-polarization weather radar. Part II: Warm- and cold-season applications. *J. Oper. Meteor.*, **1**, 243–264, https://doi.org/10.15191/nwajom.2013.0120.

——, and A. V. Ryzhkov, 2009: Storm-relative helicity revealed from polarimetric radar measurements. *J. Atmos. Sci.*, **66**, 667–685, https://doi.org/10.1175/2008JAS2815.1.

Lemon, L. R., 1976: The flanking line, a severe thunderstorm intensification source. *J. Atmos. Sci.*, **33**, 686–694, https://doi.org/10.1175/1520-0469(1976)033<0686:TFLAST>2.0.CO;2.

Lin, Y. L., S. Chiao, T. A. Wang, M. L. Kaplan, and R. P. Weglarz, 2001: Some common ingredients for heavy orographic rainfall. *Wea. Forecasting*, **16**, 633–660, https://doi.org/10.1175/1520-0434(2001)016<0633:SCIFHO>2.0.CO;2.

Loney, M. L., D. S. Zrnić, J. M. Straka, and A. V. Ryzhkov, 2002: Enhanced polarimetric radar signatures above the melting level in a supercell storm. *J. Appl. Meteor.*, **41**, 1179–1194, https://doi.org/10.1175/1520-0450(2002)041<1179:EPRSAT>2.0.CO;2.

Lyman, R. E., T. A. Schroeder, and G. M. Barnes, 2005: The heavy rain event of 29 October 2000 in Hana, Maui. *Wea. Forecasting*, **20**, 397–414, https://doi.org/10.1175/WAF868.1.

Maddox, R. A., and C. A. Doswell III, 1982: An examination of jet stream configurations, 500 mb vorticity advection, and low-level thermal advection patterns during extended periods of intense convection. *Mon. Wea. Rev.*, **110**, 184–197, https://doi.org/10.1175/1520-0493(1982)110<0184:AEOJSC>2.0.CO;2.

Markowski, P. M., and Y. Richardson, 2010: *Mesoscale Meteorology in Midlatitudes.* Wiley-Blackwell, 430 pp.

——, and N. Dotzek, 2011: A numerical study of the effects of orography on supercells. *Atmos. Res.*, **100**, 457–478, https://doi.org/10.1016/j.atmosres.2010.12.027.

Morrison, H., J. M. Peters, A. C. Varble, W. M. Hannah, and S. E. Giangrande, 2020: Thermal chains and entrainment in cumulus updrafts. Part I: Theoretical description. *J. Atmos. Sci.*, **77**, 3637–3660, https://doi.org/10.1175/JAS-D-19-0243.1.

Morrison, I., S. Businger, F. Marks, P. Dodge, and J. A. Businger, 2005: An observational case for the prevalence of roll vortices in the hurricane boundary layer. *J. Atmos. Sci.*, **62**, 2662–2673, https://doi.org/10.1175/JAS3508.1.

Mulholland, J. P., S. W. Nesbitt, and R. J. Trapp, 2019: A case study of terrain influences on upscale convective growth of a

supercell. *Mon. Wea. Rev.*, **147**, 4305–4324, https://doi.org/10.1175/MWR-D-19-0099.1.

Murphy, M. J., Jr., and S. Businger, 2011: Orographic influences on an Oahu flood. *Mon. Wea. Rev.*, **139**, 2198–2217, https://doi.org/10.1175/2010MWR3357.1.

Nielsen, E. R., and R. S. Schumacher, 2018: Dynamical insights into extreme short-term precipitation associated with supercells and mesovortices. *J. Atmos. Sci.*, **75**, 2983–3009, https://doi.org/10.1175/JAS-D-17-0385.1.

——, and ——, 2020a: Dynamical mechanisms supporting extreme rainfall accumulations in the Houston "Tax Day" 2016 flood. *Mon. Wea. Rev.*, **148**, 83–109, https://doi.org/10.1175/MWR-D-19-0206.1.

——, and ——, 2020b: Observations of extreme short-term precipitation associated with supercells and mesovortices. *Mon. Wea. Rev.*, **148**, 159–182, https://doi.org/10.1175/MWR-D-19-0146.1.

——, G. R. Herman, R. C. Tournay, J. M. Peters, and R. S. Schumacher, 2015: Double impact: When both tornadoes and flash floods threaten the same place at the same time. *Wea. Forecasting*, **30**, 1673–1693, https://doi.org/10.1175/WAF-D-15-0084.1.

Perica, S., and Coauthors, 2011: *Precipitation-Frequency Atlas of the United States*. Vol. 4, version 3: Hawaiian Islands, NOAA Atlas 14, NOAA, 103 pp., https://www.weather.gov/media/owp/hdsc_documents/Atlas14_Volume4.pdf.

Pessi, A. T., and S. Businger, 2009: The impact of lightning data assimilation on a winter storm simulation over the North Pacific Ocean. *Mon. Wea. Rev.*, **137**, 3177–3195, https://doi.org/10.1175/2009MWR2765.1.

Peters, J. M., C. J. Nowotarski, and H. Morrison, 2019: The role of vertical wind shear in modulating maximum supercell updraft velocities. *J. Atmos. Sci.*, **76**, 3169–3189, https://doi.org/10.1175/JAS-D-19-0096.1.

——, ——, J. P. Mulholland, and R. L. Thompson, 2020a: The influences of effective inflow layer streamwise vorticity and storm-relative flow on supercell updraft properties. *J. Atmos. Sci.*, **77**, 3033–3057, https://doi.org/10.1175/JAS-D-19-0355.1.

——, ——, and G. L. Mullendore, 2020b: Are supercells resistant to entrainment because of their rotation? *J. Atmos. Sci.*, **77**, 1475–1495, https://doi.org/10.1175/JAS-D-19-0316.1.

——, H. Morrison, A. C. Varble, W. M. Hannah, and S. E. Giangrande, 2020c: Thermal chains and entrainment in cumulus updrafts. Part II: Analysis of idealized simulations. *J. Atmos. Sci.*, **77**, 3661–3681, https://doi.org/10.1175/JAS-D-19-0244.1.

Ramage, C. S., 1995: Forecasters guide to tropical meteorology (AWS TR 240 updated). AWS/TR-95/001, Air Weather Service, U.S. Air Force, AWSTL, 392 pp.

Raymond, D. J., 1978: Instability of the low-level jet and severe storm formation. *J. Atmos. Sci.*, **35**, 2274–2280, https://doi.org/10.1175/1520-0469(1978)035<2274:IOTLLJ>2.0.CO;2.

Robinson, T. E., and S. Businger, 2019: A novel method for modeling lowest-level vertical motion. *Wea. Forecasting*, **34**, 943–957, https://doi.org/10.1175/WAF-D-18-0064.1.

Rosenfeld, D., D. B. Wolff, and D. Atlas, 1993: General probability-matched relations between radar reflectivity and rain rate. *J. Appl. Meteor.*, **32**, 50–72, https://doi.org/10.1175/1520-0450(1993)032<0050:GPMRBR>2.0.CO;2.

Rotunno, R., and J. B. Klemp, 1982: The influence of the shear-induced pressure gradient on thunderstorm motion. *Mon. Wea. Rev.*, **110**, 136–151, https://doi.org/10.1175/1520-0493(1982)110<0136:TIOTSI>2.0.CO;2.

Sachidananda, M., and D. S. Zrnić, 1987: Rain rate estimates from differential polarization measurements. *J. Atmos. Oceanic Technol.*, **4**, 588–598, https://doi.org/10.1175/1520-0426(1987)004<0588:RREFDP>2.0.CO;2.

Said, R., and M. Murphy, 2016: GLD360 upgrade: Performance analysis and applications. *24th Int. Lightning Detection Conf. 2016/Sixth Int. Lightning Meteorology Conf.*, San Diego, CA, ILDC/ILMC, https://training.weather.gov/wdtd/courses/woc/severe/data-fusion/lightning/sat-ltg-prod/story_content/external_files/Said_Murphy_2016.pdf.

Schroeder, T. A., 1977: Meteorological analysis of an Oahu flood. *Mon. Wea. Rev.*, **105**, 458–468, https://doi.org/10.1175/1520-0493(1977)105<0458:MAOAOF>2.0.CO;2.

Stolz, D. C., S. Businger, and A. Terpstra, 2014: Refining the relationship between lightning and convective rainfall over the ocean. *J. Geophys. Res. Atmos.*, **119**, 964–981, https://doi.org/10.1002/2012JD018819.

Thompson, R. L., C. M. Mead, and R. Edwards, 2007: Effective storm-relative helicity and bulk shear in supercell thunderstorm environments. *Wea. Forecasting*, **22**, 102–115, https://doi.org/10.1175/WAF969.1.

Trenberth, K. E., 1978: On the interpretation of the diagnostic quasi-geostrophic omega equation. *Mon. Wea. Rev.*, **106**, 131–137, https://doi.org/10.1175/1520-0493(1978)106<0131:OTIOTD>2.0.CO;2.

Uccellini, L. W., and D. R. Johnson, 1979: The coupling of upper and lower tropospheric jet streaks and implications for the development of severe convective storms. *Mon. Wea. Rev.*, **107**, 682–703, https://doi.org/10.1175/1520-0493(1979)107<0682:TCOUAL>2.0.CO;2.

——, and P. J. Kocin, 1987: The interaction of jet-streak circulations during heavy snow events along the East Coast of the United States. *Wea. Forecasting*, **2**, 289–308, https://doi.org/10.1175/1520-0434(1987)002<0289:TIOJSC>2.0.CO;2.

Warren, R. A., H. Richter, H. A. Ramsay, S. T. Siems, and M. J. Manton, 2017: Impact of variations in upper-level shear on simulated supercells. *Mon. Wea. Rev.*, **145**, 2659–2681, https://doi.org/10.1175/MWR-D-16-0412.1.

Weisman, M. L., and J. B. Klemp, 1982: The dependence of numerically simulated convective storms on vertical wind shear and buoyancy. *Mon. Wea. Rev.*, **110**, 504–520, https://doi.org/10.1175/1520-0493(1982)110<0504:TDONSC>2.0.CO;2.

——, and ——, 1984: The structure and classification of numerically simulated convective storms in directionally varying wind shears. *Mon. Wea. Rev.*, **112**, 2479–2498, https://doi.org/10.1175/1520-0493(1984)112<2479:TSACON>2.0.CO;2.

——, and R. Rotunno, 2000: The use of vertical wind shear versus helicity in interpreting supercell dynamics. *J. Atmos. Sci.*, **57**, 1452–1472, https://doi.org/10.1175/1520-0469(2000)057<1452:TUOVWS>2.0.CO;2.

Whiteman, C. D., X. Bian, and S. Zhong, 1997: Low-level jet climatology from enhanced rawinsonde observations at a site in the southern Great Plains. *J. Appl. Meteor.*, **36**, 1363–1376, https://doi.org/10.1175/1520-0450(1997)036<1363:LLJCFE>2.0.CO;2.